The Astrophysical Journal, 801:133 (18pp), 2015 March 10 doi:10.1088/0004-637X/801/2/133

SPECTROSCOPIC CONFIRMATION OF AN ULTRAMASSIVE AND COMPACT GALAXY AT $z = 3.35$: A DETAILED LOOK AT AN EARLY PROGENITOR OF LOCAL GIANT ELLIPTICALS

Z. Cemile Marsan[1], Danilo Marchesini[1], Gabriel B. Brammer[2], Mauro Stefanon[3], Adam Muzzin[4], Alberto Fernández-Soto[5,6], Stefan Geier[7], Kevin N. Hainline[8], Huib Intema[9], Alexander Karim[10], Ivo Labbé[4], Sune Toft[11], and Pieter G. van Dokkum[12]

[1] Department of Physics and Astronomy, Tufts University, Medford, MA 02155, USA
[2] Space Telescope Science Institute, 3700 San Martin Drive, Baltimore, MD 21218, USA
[3] Physics and Astronomy Department, University of Missouri, Columbia, MO 65211, USA
[4] Leiden Observatory, Leiden University, P.O. Box 9513, NL-2300 RA Leiden, The Netherlands
[5] Instituto de Física de Cantabria (CSIC-Universidad de Cantabria), Avda. de los Castros s/n, E-39005-Santander, Spain
[6] Unidad Asociada Observatori Astronòmic (IFCA-Universitat de València), C. Catedrático José Beltrán 2, E-46980-Paterna, Spain
[7] Instituto de Astrofísica de Canarias (IAC), E-38205 La Laguna, Tenerife, Spain
[8] Department of Physics and Astronomy, Dartmouth College, Hanover, NH 03755, USA
[9] National Radio Astronomy Observatory, 1003 Lopezville Road, Socorro, NM 87801-0387, USA
[10] Argelander-Institut für Astronomie, Universität Bonn, Auf dem Hügel 71, D-53121 Bonn, Germany
[11] Dark Cosmology Centre, Niels Bohr Institute, University of Copenhagen, Juliane Maries Vej 30, DK-2100 Copenhagen, Denmark
[12] Department of Astronomy, Yale University, New Haven, CT 06511, USA
Received 2014 May 29; accepted 2015 January 19; published 2015 March 12

ABSTRACT

We present the first spectroscopic confirmation of an ultramassive galaxy at redshift $z > 3$ using data from Keck-NIRSPEC, VLT-X-shooter, and GTC-Osiris. We detect strong [O III] and Lyα emission, and weak [O II], C IV, and He II, placing C1-23152 at a spectroscopic redshift of $z_{\rm spec} = 3.351$. The modeling of the emission-line-corrected spectral energy distribution (SED) results in a best-fit stellar mass of $M_* = 3.1^{+0.6}_{-0.7} \times 10^{11}\,M_\odot$, a star formation rate of $<7\,M_\odot\,{\rm yr}^{-1}$, and negligible dust extinction. The stars appear to have formed in a short intense burst ~300–500 Myr prior to the observation epoch, setting the formation redshift of this galaxy at $z \sim 4.1$. From the analysis of the line ratios and widths and the observed flux at 24 μm, we confirm the presence of a luminous hidden active galactic nucleus (AGN), with bolometric luminosity of $\sim 10^{46}\,{\rm erg\,s}^{-1}$. Potential contamination of the observed SED from the AGN continuum is constrained, placing a lower limit on the stellar mass of $2 \times 10^{11}\,M_\odot$. *HST*/WFC3 H_{160} and ACS I_{814} images are modeled, resulting in an effective radius of $r_e \sim 1$ kpc in the H_{160} band and a Sérsic index $n \sim 4.4$. This object may be a prototype of the progenitors of local most massive elliptical galaxies in the first 2 Gyr of cosmic history, having formed most of its stars at $z > 4$ in a highly dissipative, intense, and short burst of star formation. C1-23152 is completing its transition to a post-starburst phase while hosting a powerful AGN, potentially responsible for the quenching of the star formation activity.

Key words: galaxies: active – galaxies: evolution – galaxies: general – galaxies: high-redshift – galaxies: stellar content – galaxies: structure

1. INTRODUCTION

One of the most fundamental questions regarding galaxy formation and evolution is when and how the most massive galaxies in the universe formed. In the current ΛCDM paradigm, the dominant structures in the universe are dark matter halos that grow out of primordial density perturbations through gravitational collapse (White & Rees 1978). Simulations and analytical models establish that this process proceeds in a hierarchical, bottom-up manner with low-mass halos forming first and subsequently growing by continued accretion and merging to form more massive halos at later times (White & Frenk 1991; Kauffmann & White 1993; Kauffmann et al. 1999). In contrast, observational studies suggest that the stellar baryonic component of halos assembles in an anti-hierarchical, top-down manner (Cowie et al. 1996; Fontanot et al. 2009).

Closely related to this issue is the intriguing finding that the number density of the most massive galaxies ($M_* > 3 \times 10^{11}\,M_\odot$) seems to evolve very little from $z \sim 4$ to $z \sim 1.5$ (Pérez-González et al. 2008; Marchesini et al. 2009, 2010; Muzzin et al. 2013b), suggesting that very massive galaxies were already in place at $z \sim 3.5$, and implying that their stellar content was assembled rapidly in the first ~1.5 Gyr of cosmic history. In contrast to the homogeneous population of massive galaxies in the nearby universe, the population of massive galaxies in the early universe is found to span a diverse range in stellar ages, star formation rates, and dust contents (Marchesini et al. 2010, 2014; Ilbert et al. 2013; Muzzin et al. 2013b; Stefanon et al. 2013; Spitler et al. 2014). Studies of stellar mass complete samples of galaxies at high redshift reveal populations of both evolved quiescent galaxies and star-forming galaxies with varying degrees of dust attenuation (Marchesini et al. 2010; Stefanon et al. 2013; Spitler et al. 2014). An additional class of dust-enshrouded and rigorously star-forming high-z massive galaxies are uncovered through detections at longer wavelengths (submillimeter galaxies [SMG]; Smail et al. 2002). The SMG population is dominated by galaxies with star formation rates (SFRs) ~10× more intense than main-sequence galaxies at these redshifts with indications of ongoing merging (Tacconi et al. 2006; Ivison et al. 2013; Fu et al. 2013).

Theoretical models of galaxy formation and evolution severely underpredict the observed number density of galaxies at $3 < z < 4$ with $\log(M_*/M_\odot) > 11.5$ (Fontanot et al. 2009;

Marchesini et al. 2009, 2010), but systematic uncertainties in both photometric redshift and stellar mass estimates remain large. While several massive SMGs have spectroscopically confirmed redshifts at $z > 3$ (e.g., Schinnerer et al. 2008; Smolčić et al. 2011; Walter et al. 2012; Toft et al. 2014), they suffer from significant uncertainties in derived stellar population parameters (Michalowski et al. 2012). Spectroscopically confirming the redshift of rest-frame optically selected galaxies is challenging as these sources are faint in the observers' optical, requiring significant exposure times at even the largest telescopes (but see Strazzullo et al. 2013 for a massive $z_{\rm spec} = 2.99$ passive galaxy).

Studies find that, of the massive galaxy population (e.g., $M_* > 10^{11}\,M_\odot$) at $z \sim 2$, approximately 40% are no longer forming stars (Whitaker et al. 2011; Brammer et al. 2011; Muzzin et al. 2013b), and this population of quiescent galaxies undergoes significant size evolution. Specifically, massive quiescent galaxies are found to be compact, particularly those with the lowest star formation rates, with sizes a factor of ~4–5x smaller at $z \sim 2$ compared to local quiescent galaxies with similar stellar masses (Daddi et al. 2005; Trujillo et al. 2006, 2007; Toft et al. 2007; Zirm et al. 2007; Cimatti et al. 2008; van Dokkum et al. 2008, 2010; Franx et al. 2008; van der Wel et al. 2008; Bezanson et al. 2009; see van der Wel et al. 2014 for the latest comprehensive analysis on the size evolution of quiescent and star-forming galaxies). It has been suggested that dry minor mergers can cause a considerable growth in size without significantly increasing the mass of the galaxy, whereas major mergers tend to increase the mass without increasing the size much (Naab et al. 2006; Trujillo et al. 2011). A consistent size evolution through minor merging can be achieved as less massive satellite galaxies deposit mass preferentially in the outer radii of more massive central galaxies (commonly referred to as *inside-out growth*). Several recent works have indeed shown that the mass at fixed inner physical radius of massive, quiescent galaxies is nearly constant, whereas the mass in the outer regions undergoes a significant increase (a factor of ~4 since $z \sim 2$), supporting the inside-out growth of massive, quiescent galaxies (e.g., van Dokkum et al. 2010; van De Sande et al. 2013; Patel et al. 2013).

In order to understand the onset and evolution of massive galaxies, several recent works have aimed at identifying the potential progenitors of compact, massive quiescent galaxies observed at $z \sim 2$, based on number density considerations (Barro et al. 2013; Stefanon et al. 2013; Patel et al. 2013; Williams et al. 2014). Two evolutionary tracks have been proposed for the formation of massive, quiescent galaxies: an early ($z > 2$) formation path of rapidly quenched compact star-forming galaxies fading into compact, quiescent galaxies that later enlarge within the quiescent phase; and a late-arrival ($z < 2$) path in which quiescent galaxies are formed through the quenching of more extended star-forming galaxies with lower mass densities (Barro et al. 2013).

Most recently, Marchesini et al. (2014) studied the evolution of the properties of the progenitors of ultramassive galaxies ($\log(M_*/M_\odot) \approx 11.8$; UMGs) at $z \sim 0$ with a semi-empirical approach using abundance matching. At $2 < z < 3$, the progenitors of local UMGs are found to be dominated by massive ($M_* \approx 2 \times 10^{11}\,M_\odot$), dusty ($A_{\rm V} \sim 1$–$2.2$ mag), and star-forming (SFR ~ 100–400 $M_\odot$ yr^{-1}) galaxies, although a small fraction (~15%) of them are found to be already quiescent at $2.5 < z < 3.0$. The $2.5 < z < 3.0$ quiescent progenitors of local UMGs are found to have properties typical of young (0.6–1 Gyr) post-starburst galaxies with little dust extinction ($A_{\rm V} \sim 0.4$ mag) and strong Balmer breaks, showing a large scatter in rest-frame $U - V$ color (~0.2 mag). The existence of such quiescent progenitors at $z = 2.75$ indicates that the early assembly of the massive end of the local quiescent redsequence must have started at $z > 3$, as also implied by archeological studies in the local universe (e.g., Thomas et al. 2005, 2010; Charlot et al. 2006).

Evidence for the existence of massive ($M_* > 10^{11}$) galaxies at $z > 3$ with suppressed star formation has been found through studies of deep near-infrared (NIR) selected catalogs (Wiklind et al. 2008; Mancini et al. 2009; Marchesini et al. 2010; Stefanon et al. 2013; Muzzin et al. 2013b; Straatman et al. 2014), with accurate photometric redshifts and well-sampled spectral energy distributions (SEDs). However, spectroscopic observations are necessary to confirm the redshifts and to better characterize the properties of these galaxies. It is also of vital importance to determine active galactic nucleus (AGN) and/or starburst contamination to the optical-to-MIR SEDs of these sources to properly constrain the high-mass end of the stellar mass function at these redshifts.

In this paper, we present the first spectroscopic confirmation of a very massive galaxy at $z > 3$, C1-23152, with a detailed investigation of its stellar population and structural properties, as well as the AGN energetics. C1-23152 is the brightest ($K = 20.3$ mag, AB) galaxy within the stellar mass complete ($M_* > 2.5 \times 10^{11}\,M_\odot$) sample of 14 galaxies at $3 < z < 4$ presented in Marchesini et al. (2010) and was initially selected from the NEWFIRM Medium-Band Survey (NMBS; Whitaker et al. 2011). C1-23152 is in the COSMOS field (Scoville et al. 2007) and has a photometric redshift $z_{\rm phot} = 3.29 \pm 0.06$ and a stellar mass of $\log(M_*/M_\odot) = 11.42$ (Marchesini et al. 2010). By combining the broad- and medium-band photometry from NMBS with optical and NIR spectroscopic data from both ground- and space-based facilities, we spectroscopically confirm the very large stellar mass of C1-23152 through detailed modeling of its SED, and provide robust evidence for the evolutionary path linking C1-23152 to local giant elliptical galaxies.

This paper is organized as follows: In Section 2, we present the observations of C1-23152, including extensive space- and ground-based spectroscopy from the ultraviolet (UV) to the NIR, as well as space-based imaging. In Section 3, we present the analysis of the spectra and the modeling of the SED, and the derivation of the structural parameters from space-based imaging. The results are summarized and discussed in Section 4. We assume $\Omega_{\rm M} = 0.3$, $\Omega_\Lambda = 0.7$, $H_0 = 70$ km s^{-1} Mpc^{-1}, and a Kroupa (2001) initial mass function (IMF) throughout the paper. All magnitudes are on the AB system.

2. DATA

2.1. Broad- and Medium-band Photometry from the NMBS

The target C1-23152 (R.A. = $10^{\rm h}00^{\rm m}27\overset{\rm s}{.}81$, decl. = $+02^{\rm d}33^{\rm m}\ 49\overset{\rm s}{.}3$; J2000) is selected from the mass-complete ($M_* > 2.5 \times 10^{11}\,M_\odot$) sample of galaxies at $3 < z < 4$ constructed from the NMBS and presented in Marchesini et al. (2010). C1-23152 lies in the COSMOS field (Scoville et al. 2007), with excellent supporting data. The NMBS photometry presented in Whitaker et al. (2011)

Table 1
Ground-based Spectroscopic Observations

Band/Arm	λ_{range} (μ)	t_{exp} (minutes)	FWHM ($''$)	Date	Width ($''$)
		Keck-NIRSPEC			
N5 (H)	1.48–1.71	75	0.7	2011 Feb 11	0.72
N7 (K)	1.94–2.37	75	0.7	2011 Feb 11	0.72
		VLT-X-shooter			
UVB	0.3–0.59	35	1.16	2011 May 27	1.0
VIS	0.53–1.02	35	1.16	2011 May 27	0.9
NIR	0.99–2.48	40	1.16	2011 May 27	0.9
		GTC-Osiris			
R1000B	0.37–0.77	42	0.9	2011 Nov	0.8
R1000B	0.37–0.77	42	1.6	2012 Feb	0.8
R1000B	0.37–0.77	45	1.0	2013 Jan	0.8

Note. λ_{range} is the wavelength range covered by the instrumental setup; t_{exp} is the on-source exposure time in minutes; FWHM is the average seeing in arcseconds of the observations. The last two columns list the nights during which the spectroscopic data were taken and the width of the used slit in arcseconds, respectively.

includes deep optical *ugriz* data from the CFHT Legacy Survey, deep *Spitzer*-IRAC and MIPS imaging (Sanders et al. 2007), deep Subaru images with the $B_J V_J r^+ i^+ z^+$ broadband filters (Capak et al. 2007), Subaru images with 12 optical intermediate-band filters from 427 to 827 nm (Taniguchi et al. 2007), JHK_S broadband imaging from the WIRCam Deep Survey (WIRDS; McCracken et al. 2010), *GALEX* photometry in the FUV (150 nm) and NUV (225 nm) passbands (Martin 2005), and NIR imaging with NEWFIRM using the five medium-band filters J_1, J_2, J_3, H_1, H_2, and broadband K from NMBS (van Dokkum et al. 2009), for a total of 37 photometric points. In the publicly released v5.1 NMBS catalog, C1-23152 is identified as C1–35502, and has total apparent magnitudes of $K_S = 20.31$ mag and $r = 23.24$ mag.

2.2. Ground-based Spectroscopy and Data Reduction

In this section we describe the ground-based spectroscopic data of C1-23152 obtained from Keck-NIRSPEC, VLT-X-shooter, and GTC-Osiris as part of follow-up programs aimed at spectroscopically confirming the existence of very massive galaxies at $z > 3$. Along with the observational techniques, we provide a summary of the data reduction. The detailed description of the data reduction and the full sample will be presented elsewhere (C. Marsan et al. 2015; in preparation). Table 1 summarizes the wavelength coverage, total exposure time, seeing, date of observations, and the slit width of the spectroscopic observations.

2.2.1. Keck-NIRSPEC

We observed C1-23152 using Keck-NIRSPEC (McLean et al. 1998) in cross-dispersed mode and the $42'' \times 0\farcs76$ slit for both N5 (H) and N7 (K) filters, obtaining a wavelength coverage of 1.48–1.71 μm and 1.94–2.37 μm, and a spectral resolution of $R = 1100$ and $R = 1500$, respectively. The observations were carried out on the night of 2011 February 11, as part of the NOAO program 2011A-0514 (PI: Marchesini) with a typical seeing of $0\farcs7$, which worsened throughout the sequence of observations due to cloudy variable weather. Observations were conducted following an ABA′B′ on-source dither pattern. The orientation of the slit was set to include a bright point source to serve as reference when analyzing and combining the two-dimensional (2D) rectified frames. The target was acquired using blind offsets from a nearby bright star. The alignment of the offset star in the slit was checked before each individual 900 s exposure and corrected when necessary. Before and after the observing sequence, a spectrophotometric standard and an AV0 star was observed for the purpose of correcting for telluric absorption and detector response.

The data reduction for the NIRSPEC observations used a combination of custom IDL scripts and standard IRAF tasks.[13] As the initial step, a bad pixel mask was created by flagging outlier pixels in dark and flat frames. The cosmic rays on the science frames were removed using L.A.Cosmic (van Dokkum 2001). The frames and their corresponding sky spectra were rotated such that the sky lines are along columns, using a polynomial to interpolate between adjacent pixels. The spectra were wavelength calibrated by fitting Gaussian profiles to the OH lines in the 2D sky spectra. Each spectrum was sky subtracted using an adjacent spectrum with the IDL routines written by George Becker. The sky-subtracted frames and the sky spectra were rectified to a linear wavelength scale. The standard star frames used to correct for atmospheric absorption and detector response were rectified and reduced in the same manner as the science frames. A one-dimensional spectrum was extracted for each telluric standard star (before and after science observations) by summing all the rows (along the spatial direction) with a flux greater than 0.1 times that of the central row. The average of the one-dimensional telluric star spectra was used to correct the 2D science and spectrophotometric star frames for telluric absorption. The one-dimensional spectrum of the spectrophotometric star was extracted in the same manner and used to create a response function for flux calibration. The 2D rectified and reduced science frames were combined by weighting according to their signal-to-noise ratio (S/N).

2.2.2. VLT-X-shooter

X-shooter is a single-object, medium-resolution echelle spectrograph with simultaneous coverage of wavelength range 0.3–2.5 μm in three arms (UVB, VIS, NIR) (D'Odorico et al. 2006). The observations of our target were carried out in queue mode as part of the ESO program 087.A-0514 (PI: Brammer) under poor seeing conditions (FWHM $\sim 1\farcs2$), following an ABA′B′ on-source dither pattern using the $11'' \times 1\farcs0$ and $11'' \times 0\farcs9$ slits for the UVB and VIS/NIR arms, respectively. This instrumental setup resulted in a spectral resolution of $R = 4200$, 8250, and 4000 for the NIR, VIS, and UVB arms, respectively. For calibration purposes, telluric and spectrophotometric standard stars were observed in the same setup as science observations.

The data reduction for the X-shooter observations used custom scripts based on the standard X-shooter reduction pipeline (Modigliani et al. 2010). The calibration steps (master

[13] IRAF is distributed by the National Optical Astronomy Observatory, which is operated by the Association of Universities for Research in Astronomy (AURA), Inc., under cooperative agreement with the National Science Foundation.

darks, order prediction, flat fields, and the 2D maps for later rectification of the spectra) were run with the default parameters in the pipeline (Goldoni 2011). After these five calibration steps, the echelle spectra were dark-subtracted, flat-fielded, and rectified, and the orders stitched (12, 15, and 16 for the UVB, VIS, and NIR arms, respectively). The sky was then subtracted using adjacent exposures. Standard star observations were reduced with the same calibration data as the science frames and used to correct for telluric absorption and detector response. A final spectrum was created by mean stacking all exposures. We refer to Geier et al. (2013) for a detailed description of reduction steps of X-shooter spectra.

2.2.3. GTC-Osiris

The target was also observed using the Gran Telescopio Canarias (GTC) with the Osiris optical spectrograph (Cepa et al. 2003) in long-slit mode with the R1000B grism (dispersion of 2.12 Å pixel^{-1}) and a 0.″8 wide slit, resulting in a spectral resolution of $R \sim 800$. Observations were carried out in queue mode under clear sky conditions under programs GTC8-11B and GTC22-12B (PI: Fernández-Soto). During the 2011/2012 winter we obtained two separate runs. The first one was acceptable (average seeing of 0.″9), but the second was below the expected quality and the data were not useful (seeing worse than 1.″5). In each of them three exposures of 840 s each were taken, using offsets of +1.″78/0″/−1.″78 along the slit. A third run in 2013 January obtained three more exposures of 900 s each, with an adequate seeing (1.″0) and using the same observing strategy. In all cases the orientation of the slit was set to include a bright point source to serve as reference when analyzing and combining the 2D rectified frames.

Data reduction was performed using the standard long-slit package in IRAF (Valdes 1992), and all previous image calibration steps (bias subtraction, trimming, flat-fielding) before the final frame combination for each separate run were also performed within IRAF. Wavelength calibration was obtained using the HgAr and Ne arclamp exposures provided by the Observatory, and the images were rectified to correct for obvious flexures along the spatial direction. An approximate flux calibration was obtained via the observations of the spectrophotometric standard stars G191-B2B and GD158-100.

2.2.4. Extraction of One-dimensional Spectra

Following Horne (1986), one-dimensional spectra were extracted by summing all adjacent lines (along the spatial direction) using weights corresponding to a Gaussian centered on the central row with an FWHM equal to the slit width used in each observation. To correct for slit losses and obtain an absolute flux calibration, spectroscopic broad/medium-band fluxes were obtained by integrating over the corresponding filter curves, and a constant scaling was applied to each spectra individually. A binned, lower-resolution spectrum with higher S/N was extracted for each spectra using optimal weighting, excluding parts of spectra contaminated by strong sky emission or strong atmospheric absorption. The resulting spectral resolutions of the binned X-shooter spectra were $R \approx 30$–45, 15–40, and 20–50 for the UVB, VIS, and NIR arms, respectively, while the spectral resolutions of the binned NIRSPEC spectra were $R \approx 30$–100 and 100–300 for the *H* and *K* bands, respectively.

2.3. ACS-G800L Grism Spectrum

C1-23152 lies within the area observed with the *Hubble Space Telescope* (*HST*) ACS G800L grism by the 3D-*HST* survey (Brammer et al. 2012); unfortunately, it lies outside of the area covered by the infrared G141 grism. The G800L grism covers the wavelength range 0.55–1.0 μm with a dispersion of 40 Å pixel^{-1} and a resolution of 80 Å for point-like sources (Kummel et al. 2011). We extract a flux-calibrated spectrum for C1-23152 using the `aXe` software (Kummel et al. 2009). The G800L spectrum of C1-23152 has no significant contamination from overlapping spectra of nearby sources and has a total integration time of 3123 s.

2.4. ACS I_{814} and WFC3 H_{160} Imaging

C1-23152 has been observed with *HST* using the WFC3 and the F160W filter (H_{160}, hereafter) as part of the *HST* Cycle 20 program GO-12990 (PI: Muzzin). Four individual H_{160} exposures were aligned and combined with the *MultiDrizzle* software (Koekemoer et al. 2002) following the procedure outlined by Skelton et al. (2014). The combined H_{160} image has an exposure time of 861 s and is drizzled to a pixel scale of 0.″03 pixel^{-1} with a point-source FWHM $\sim$ 0.″15. ACS F814W (I_{814}, hereafter) imaging of C1-23152 is also available from the *HST* Cycle 12 program GO-9822 (Scoville et al. 2007).

3. ANALYSIS

3.1. Emission Features and Spectroscopic Redshift

The nebular emission lines that we set out to measure were Lyα, C IV λ1549, He II λ1640, [O II] λ3727, Hβ, and [O III] $\lambda\lambda$ 4959, 5007. Upon visual inspection of the reduced 2D spectra, the Lyα (both X-shooter and Osiris) and [O III] $\lambda\lambda$4959, 5007 lines were easily identified.

The emission lines (except Lyα) were fit by a symmetric Gaussian profile plus a local continuum. In the case of the [O III] doublet (easily identifiable by eye), identical redshift and FWHM were assumed with the ratio of the amplitudes [O III] λ4959/[O III] λ5007 fixed to 1:3.

The [O II] $\lambda\lambda$3726, 3729 line doublet in the *H* band was fit as a single Gaussian emission line, based on S/N and spectral resolution considerations. The analysis of [O II] λ3727 and Hβ lines was more complicated due to significant sky residuals at their locations. Therefore, their measurements were carried out in multiple approaches. First, we fit both lines with redshift and FWHM (velocity) fixed at the best-fit values obtained from [O III]. We then left the width as a free parameter. The [O II] line is only marginally detected in emission, and we obtained a 3σ upper limit for the Hβ emission by assuming the amplitude of the emission line to be three times the uncertainty in the local continuum. C IV is detected in emission blueshifted with respect to the redshift derived from [O III] (this is discussed later in this section). He II is marginally detected with a possible signature of self-absorption (also seen for Lyα; see below). We determined the redshift of the self-absorption component using the central wavelength of the best-fit Gaussian line profile in absorption on top of an emission component.

A Monte Carlo approach was used to measure the uncertainties in the centroid, flux, and width. For each spectra, 1000 simulated spectra were created by perturbing the flux at each wavelength of the true spectrum by a Gaussian random amount with the standard deviation set by the level of the 1σ

Table 2
Spectral Line Properties

Feature	λ_{lab} (Å)	λ_{obs} (Å)	σ_{obs} (Å)	σ_{inst} (Å)	σ_{int} (Å)	z	FWHM (km s^{-1})	EW_{obs} (Å)	L (10^{42} ergs s^{-1})	χ^2_{red}
					Keck-NIRSPEC					
O III	4960.295	$21578.9^{+3.91}_{-7.67}$	$25.1^{+6.66}_{-6.60}$	6.02	$24.4^{+6.66}_{-6.60}$	$3.351^{+0.001}_{-0.002}$	$798.0^{+218.0}_{-215.9}$	$37.9^{+7.3}_{-6.6}$	$5.5^{+5.0}_{-2.9}$	0.31
O III	5008.240	$21792.0^{+3.91}_{-7.67}$	$25.1^{+6.66}_{-6.60}$	6.02	$24.4^{+6.66}_{-6.60}$	$3.351^{+0.001}_{-0.002}$	$790.2^{+215.9}_{-214.90}$	$113.8^{+21.9}_{-19.8}$	$16.5^{+15.1}_{-8.8}$	0.31
O II[a]	3727.80	16220.5	19.13	6.24	18.08	3.351	786.9	$54.4^{+29.2}_{-23.4}$	$7.54^{+10.1}_{-4.17}$	0.18
Hβ[a]	4862.68	21158.7	24.4	6.24	23.6	3.351	786.9	$-14.7^{+13.9}_{-14.6}$	$\leqslant 0.88$	0.30
					VLT-X-shooter					
Lyα	1215.24	5290.47±0.57	6.93±0.6	0.45	6.92±0.6	3.353±0.001	923.0 ± 79.3	466.4 ± 231.3	46.2 ± 6.8	0.47
$Ly\alpha_{self-abs}$	1215.24	$5290.58^{+1.53}_{-0.73}$	…	…	…	$3.354^{+0.001}_{-0.001}$	…	…	…	0.53
Lyα1	…	$5284.6^{+0.70}_{-0.57}$	$1.75^{+0.76}_{-1.15}$	0.45	$1.69^{+0.76}_{-1.15}$	$3.349^{+0.001}_{-0.001}$	…	…	…	0.50
Lyα2	…	$5293.6^{+1.40}_{-1.71}$	$8.01^{+2.46}_{-2.28}$	0.45	$8.00^{+2.46}_{-2.28}$	$3.356^{+0.001}_{-0.002}$	…	…	…	0.50
He II	1640.405	$7132.4^{+4.09}_{-3.64}$	$5.49^{+2.52}_{-3.27}$	0.34	$5.48^{+2.52}_{-3.27}$	$3.348^{+0.003}_{-0.002}$	$542.1^{+249.5}_{-323.4}$	$48.3^{+22.8}_{-26.8}$	$8.46^{+10.6}_{-8.0}$	0.36
He $II_{self-abs}$	1640.405	$7132.5^{+4.09}_{-3.64}$	…	…	…	$3.348^{+0.001}_{-0.001}$	…	…	…	0.35
O III	4960.295	$21570.0^{+15.5}_{-8.10}$	$18.16^{+7.32}_{-9.82}$	1.74	$18.08^{+7.32}_{-9.82}$	$3.349^{+0.003}_{-0.002}$	$591.6^{+239.4}_{-239.4}$	$80.1^{+17.7}_{-36.4}$	$15.0^{+5.8}_{-1.4}$	0.49
O III	5008.240	$21778.5^{+15.5}_{-8.10}$	$18.16^{+7.32}_{-9.82}$	1.74	$18.08^{+7.32}_{-9.82}$	$3.349^{+0.003}_{-0.002}$	$585.9^{+237.3}_{-318.3}$	$240.2^{+53.1}_{-109.0}$	$45.0^{+17.0}_{-4.3}$	0.49
					GTC-Osiris					
Lyα	1215.24	5289.14±0.31	5.32±0.32	3.47	4.03±0.32	3.352±0.001	538.4 ± 42.1	485.0 ± 145.0	34.3 ± 2.7	1.53
$Ly\alpha_{self-abs}$	1215.24	$5288.3^{+0.6}_{-0.7}$	…	…	…	$3.352^{+0.001}_{-0.001}$	…	…	…	1.89
Lyα1	…	$5283.1^{+0.5}_{-0.6}$	$2.57^{+0.99}_{-0.84}$	3.47	…	$3.347^{+0.001}_{-0.001}$	…	…	…	1.63
Lyα2	…	$5293.9^{+0.6}_{-0.6}$	$2.94^{+0.68}_{-0.53}$	3.47	…	$3.356^{+0.001}_{-0.001}$	…	…	…	1.63
C IV	1549.48	$6732.6^{+2.3}_{-1.9}$	$7.44^{+2.04}_{-1.85}$	4.35	$6.04^{+2.04}_{-1.85}$	$3.345^{+0.002}_{-0.001}$	$633.6^{+214.0}_{-194.1}$	$40.8^{+21.7}_{-10.3}$	$3.35^{+1.17}_{-1.71}$	1.44
$C\ IV_{abs}$	1549.48	6706.1 ± 1.9	$6.06^{+2.37}_{-4.14}$	4.35	$4.23^{+2.37}_{-4.14}$	3.328 ± 0.001	$445.4^{+249.6}_{-436.0}$	$-24.0^{+16.0}_{-8.4}$	…	1.44

Notes. λ_{lab} is the laboratory rest-frame wavelength of the targeted spectral lines; λ_{obs} is the observed wavelength of the corresponding lines; σ_{obs} is the observed width of the modeled spectral lines; σ_{inst} is the instrumental width determined from the sky lines; σ_{int} is the intrinsic width of the spectral lines in the observed frame; z is the derived redshift; FWHM is the intrinsic velocity width of the spectral lines; EW_{obs} is the observed equivalent widths of the spectral lines; and L is the integrated line luminosity calculated using the adopted systemic redshift $z_{spec} = 3.351$. χ^2_{red} is the reduced χ^2 values for corresponding emission line fits. Listed errors correspond to the 1σ uncertainties derived from the Monte Carlo simulations.

[a] Denotes fits to emission lines with redshift *and* line width fixed to that of [O III].

error spectrum. Line measurements were obtained from the simulated spectra in the same manner as the actual data. We compute the formal lower and upper confidence limits by integrating the probability distribution of each parameter (centroid, width, continuum, and emission line flux) from the extremes until the integrated probability is equal to 0.1585.

The best-fit values of the modeled spectral lines are listed in Table 2, with the quoted uncertainties corresponding to the 1σ errors estimated from the Monte Carlo simulations.

The profile of the Lyα emission is observed to be asymmetrically double-peaked in both the X-shooter and Osiris spectra, indicative of self-absorption, and we analyzed it with a number of approaches. We initially fit each peak independently with a Gaussian profile, assuming a constant continuum. Then, in order to account for the self-absorption, we fit the observed spectra simultaneously with two Gaussians, one in emission and the other in absorption. Finally, we fit the wings of the Lyα emission with a single Gaussian after masking the self-absorbed region between the two peaks in order to obtain the line width of the emission line. We determine that the higher-S/N X-shooter spectrum samples the wings of the Lyα emission line better, resulting in an FWHM of $\sim 923.0 \pm 79.3$ km s^{-1}, comparable with the widths found in other high-z Type II QSOs (Norman et al. 2002; Alexandroff et al. 2013).

In Figure 1 we show the observed one-dimensional spectra around the regions of the considered spectral lines. The regions of the spectra significantly affected by sky lines (shown by gray filled areas) were excluded from the line profile modeling. The redshift of a galaxy's nebular lines (e.g., [O II] λ3727, Hβ, [O III] λλ4959, 5007) is expected to be nearly equal to the redshift of its stars, i.e., the gas responsible for the nebular emission should always lie close to hot stars. We therefore choose the redshift of the [O III] emission lines, $z_{spec} = 3.351^{+0.001}_{-0.002}$, to be the systemic redshift of the galaxy.

Due to the resonant nature of the transition in neutral hydrogen, the interpretation of the origin of the Lyα emission is non-trivial (Verhamme et al. 2006; Kulas et al. 2012). In Figure 2 we show the spectroscopic redshifts and corresponding uncertainties for all observed spectral lines. We note that the prominent double-peaked Lyα in both the X-shooter and Osiris spectra brackets the systemic redshift of the galaxy, and the redshifts of the self-absorbing material obtained from both the Lyα and He II are also consistent with the systemic redshift derived from [O III].

We marginally detect an emission line with a potential P Cygni profile at 6732 Å in the Osiris spectrum, which we interpret as C IV λ1549 emission blueshifted with respect to the systemic redshift by 425 km s^{-1}. P Cygni line profiles are powerful diagnostics of outflow kinematics (Spoon

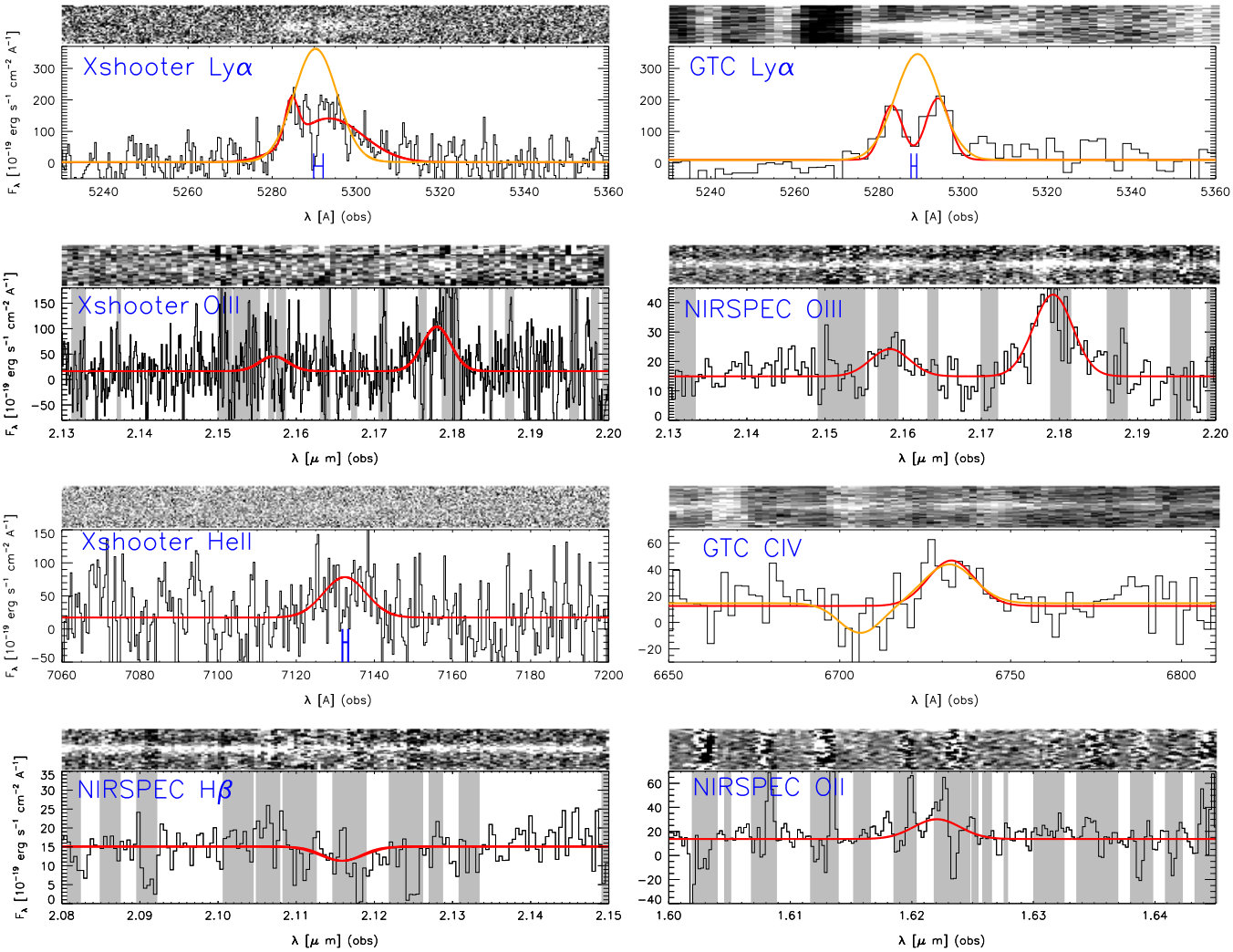

Figure 1. Observed one-dimensional and two-dimensional spectra in the region around the considered spectral features. The red solid curves represent the best-fit Gaussian profiles to the emission lines in 1D spectra. The orange solid curves in the top panels represent the best-fit single Gaussian profile after masking the self-absorbed region between the two Lyα peaks. The orange solid curve in the C IV panel represents best-fit P Cygni profile. The gray shaded regions indicate regions of the spectra significantly affected by telluric sky lines. The best-fit central wavelength and 1σ uncertainty of the central wavelength of the self-absorption component of Lyα and He II are indicated by the blue brackets in the corresponding panels.

et al. 2013). We fit the observed P Cygni profile of C IV with a component in emission and a blueshifted broad component in absorption. The absorption feature of the P Cygni profile is blueshifted by $\sim$1160 $\pm$ 130 km s^{-1} with respect to the emission component. We note that high-ionization emission lines blueshifted with respect to low-ionization emission lines have been previously observed in (particularly radio-quiet) luminous quasars by Richards et al. (2011), who argue that the apparent *blueshift* with respect to the systemic redshift might be the result of preferential reduction/obscuration of the red wing of the C IV emission line. We however stress that the C IV detection in the Osiris spectrum is only marginally significant, and that C IV emission is not detected in the X-shooter spectrum; therefore, caution is required when interpreting the ambiguous C IV detection. Although a C IV emission feature is often used as evidence for the identification of AGNs (Daddi et al. 2004; Hainline et al. 2011), it has been found to be missing in $z \sim 2.5$ AGNs with moderately broad (FWHM $\sim$1430 km s^{-1}) Lyα emission (Hall et al. 2004).

We calculated the fluxes of the observed emission lines by integrating the fitted Gaussian profiles, with uncertainties determined using the 1σ standard deviations derived from Monte Carlo simulations of the amplitude and velocity width of the fits. The line luminosities estimated using the adopted systemic redshift are listed in Table 2, which also lists the line velocities (FWHM) corrected for the instrumental profile (determined from the width of the sky lines). The [O III] line width is FWHM$_{[\mathrm{O\,III}]} \approx 790 \pm 220$ km s^{-1}, in good agreement with the line widths observed in low-redshift Seyfert II galaxies (FWHM < 1200 km s^{-1}; Hao et al. 2005). The Lyα line width is slightly broader, with FWHM$_{\mathrm{Ly}\alpha} \approx 920 \pm 80$ km s^{-1}.

3.2. SED Modeling and Stellar Population Properties

In this section we present the modeling of the observed SED of C1-23152 obtained by combining the photometry from NMBS and the spectra from the UV to the NIR, and we present the derived properties of its stellar population.

In order to robustly constrain the stellar population parameters, all spectra and photometry must be corrected for contamination from nebular emission lines. We determined the necessary emission-line corrections for all observed

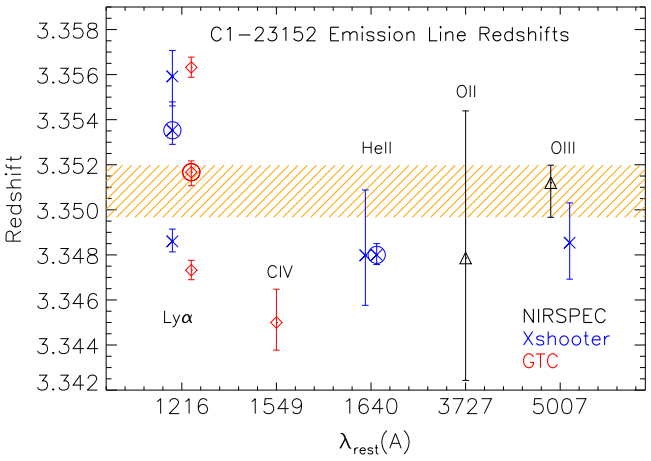

Figure 2. Spectroscopic redshifts obtained from different emission lines. *Blue crosses* show the redshifts of spectral features measured in the X-shooter spectra; *red diamonds* show the redshifts of spectral features measured in the Osiris spectra; *black triangles* indicate the redshifts of spectral features measured in the NIRSPEC spectra. Open circles represent the redshifts measured from the self-absorption features in the Lyα and He II lines. The orange hatched region indicates the adopted systemic redshift for C1-23152 based on the higher S/N NIRSPEC [O III] detection, i.e., $z_{\rm spec} = 3.351^{+0.001}_{-0.002}$.

photometries by comparing the observed-frame equivalent width of each emission line to the bandwidth of the corresponding filter. We found that the contributions due to [O II] and [O III] amount to <5% in the NMBS H_1, H, K, and K_S bands. The contributions due to Lyα emission were much more significant in the g and V broadbands, ~60% and ~90%, respectively. We also removed the photometry belonging to the medium-band IA527 (Subaru) from the fitting routine as this band was completely dominated by the Lyα emission.

We estimated the stellar population properties by fitting the binned, low-resolution UVB, visual, and NIR X-shooter, NIRSPEC, and ACS grism spectra in combination with the broadband and medium-band photometry with stellar population synthesis (SPS) models. We excluded the Osiris spectrum due to its lower S/N compared to the binned X-shooter spectrum and the photometry in the same wavelength regime. We used FAST (Fitting and Assessment of Synthetic Templates; Kriek et al. 2009) to model and fit a full grid in metallicity, dust content, age, and star formation timescale. We investigated different star formation histories (SFHs), i.e., the exponentially declining, the delayed-exponentially declining, and the truncated SFHs. We adopted SPS models from both Bruzual & Charlot (2003) and Maraston (2005) (BC03 and MA05, hereafter), and we assumed the Kroupa (2001) IMF and the Calzetti et al. (2000) extinction law. The age range allowed was between 10 Myr and 1.9 Gyr (the maximum age of the universe at the redshift of the galaxy) with a step size of 0.1 dex. We adopted a grid for τ between 3.16 Myr and 10 Gyr in steps of 0.10 dex. We allowed the dust attenuation (A_V) to range from 0 to 3 mag with step size of 0.01 mag. Metallicity can vary between $Z = 0.004$, 0.08, 0.02, 0.05 or $Z = 0.001$, 0.01, 0.02, 0.04 for the BC03 and the MA05 templates, respectively. We initially modeled the observed SED with the metallicity as a free parameter, and then we repeated the modeling by treating the metallicity as a systematic uncertainty by fixing it at the available values.

Figure 3 shows the observed SED blueshifted to the rest frame of the galaxy with the MA05 and BC03 SPS models and an exponentially declining SFH. The results of the SED modeling and the corresponding 3σ errors are listed in Table 3.

As shown by the values in Table 3, the median stellar mass derived adopting the BC03 models is $\log(M_*/M_\odot) = 11.49 \pm 0.08$. The error budget is dominated by the systematic uncertainties due to different SED-modeling assumptions. Nonetheless, given the very highquality and sampling of the SED of C1-23152, different modeling assumptions affect the derived stellar mass by at most ±0.08 dex, i.e., <20%. Independently of the SED-modeling assumptions, the best-fit dust attenuation is zero, with a 3σ upper limit of ~0.4 mag when the observed SED is modeled with MA05 SPS models, a delayed-exponentially declining SFH, and supersolar metallicity. This combination of SED-modeling assumptions also results in the largest 3σ upper limit for the SFR, i.e., 7 $M_\odot$ yr^{-1}. However, most of the other combinations of SED-modeling assumptions result in low or negligible SFRs, with a more typical 3σ upper limit of 2–5 $M_\odot$ yr^{-1}. The best-fit SFR-weighted mean stellar age $\langle t \rangle_{\rm SFR}$ of the galaxy (as defined in Föster Scheriber et al. 2004) is 350 Myr when adopting BC03 models and a best-fit solar metallicity, and a factor of 2 smaller when adopting MA05 models with a best-fit super-solar metallicity. We note that the stellar age can vary by as much as ±0.2 dex depending on the metallicity. The preferred timescale of the duration of the burst (τ) is always very short, <70 Myr at 3σ, with a typical best-fit value of ~50 Myr. We finally note that the value of τ is found to be systematically lower by as much as a factor of ~8 when the MA 05 models are assumed. The best-fit stellar age of ~400 Myr implies a formation redshift of $z_{\rm form} \sim 4.1$.

It should be noted that the stellar population parameters derived above likely suffer from additional systematic errors due to uncertainties in the modeling of the evolution of stellar populations (e.g., differences in SPS models; see, e.g., Marchesini et al. 2009; Conroy et al. 2009, 2010; Conroy & Gunn 2010) and variations in the assumed IMF. Conroy et al. (2009) find that stellar mass estimates of $z \sim 2$ luminous red galaxies can vary by ~0.6 dex due to different models of the advanced stages of stellar evolution, particularly the thermally pulsating asymptotic branch (TP-AGB) phase. Assuming a different IMF will also affect the calculated stellar mass as this affects the stellar mass-to-light ratio (M/L), with it being more sensitive to age for more top-heavy IMFs. For example, using a relatively more bottom-heavy Salpeter (1955) IMF than the adopted Kroupa (2001) would result in stellar masses ~0.2 dex higher. Recently, several studies (e.g., Conroy & van Dokkum 2012; Conroy et al. 2013; Spiniello et al. 2014) concluded that the IMF becomes increasingly bottom heavy toward galaxies characterized by larger velocity dispersion. Given the inferred large stellar mass and its compact size (~1 kpc; see Section 3.8), it is plausible that a super-Salpeter IMF may be more appropriate for C1-23152, resulting in an even larger stellar mass (by ~0.3 dex with respect to Kroupa; Conroy & van Dokkum 2012).

Compared to the stellar population parameters derived in Marchesini et al. (2010) for C1-23152 based only on the NMBS photometry, we find that the stellar mass is larger by ~0.07 dex, SFR larger by ~1.5 dex (but well within the quoted uncertainties listed in Marchesini et al. 2010), and the stellar age older by ~0.5 dex.

Given the evidence for more complex SFHs in high-z galaxies found in literature (e.g., Papovich et al. 2011;

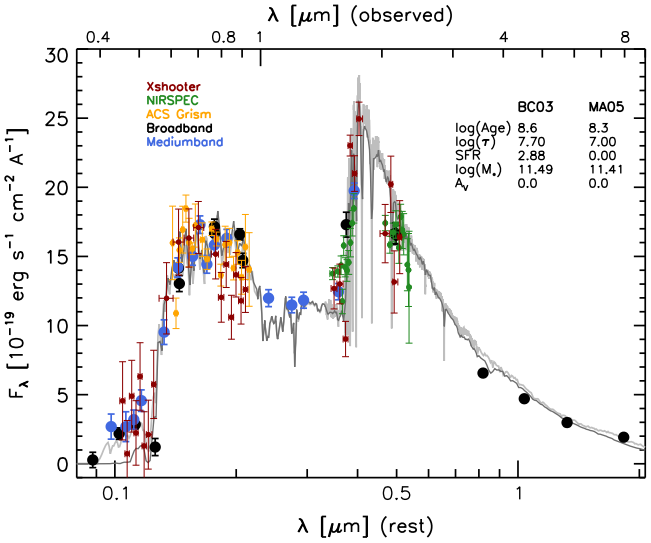

Figure 3. Observed SED from the combination of the medium- (blue filled circles) and broad-band (black filled circles) NMBS photometry and the binned spectra (NIRSPEC in green; ACS grism in orange; and X-shooter in maroon) redshifted to the rest frame. The light and dark gray curves represent the best-fit models adopting the BC03 and MA05 stellar population models, respectively, with an exponentially declining SFH and free metallicity. Best-fit stellar population properties of the BC03 and MA05 models are indicated.

Finkelstein et al. 2011), we also consider a scenario in which a recent burst of star formation is triggered through gas infall. To investigate this, we fit the observed SED with libraries created using GALAXEV (Bruzual & Charlot 2003) for two-component SFHs. We use exponentially declining SFHs (with $\log(\tau\ [\mathrm{yr}]) = 7.1, 7.3, 7.5, 7.7, 7.9$) to model the old stellar population accounting for the majority of the galaxy's stellar mass, and introduce a burst contributing a fraction of the stellar mass (5%, 10%, 20%, 30%, or 50%) when the old stellar population reaches an age of 0.2, 0.3, 0.7, 1.0, 1.2, or 1.4 Gyr. Each SFH is modeled for four different metallicities ($Z = 0.004, 0.008, 0.02, 0.05$). We used FAST to fit the observed SED using these libraries in two manners. First, we modeled the observed SED with only an upper limit restriction to the age of the stellar population dictated by the age of the universe at $z = 3.3512$. In this case, the modeled fits for the SFHs with $\Delta t_{\mathrm{burst}} \geqslant 0.3$ Gyr are essentially identical, with $\log(M_*/M_\odot) = 11.42$, $\mathrm{SFR} = 4\,M_\odot\,\mathrm{yr}^{-1}$, and an age of ~250 Myr, without bursts taking place. The only SFHs in which the fits favor the occurence of the burst are the $\Delta t_{\mathrm{burst}} = 0.2$ Gyr models. The median stellar mass is $\log(M_*/M_\odot) = 11.48 \pm 0.2$, and $\mathrm{SFR} = 1.5 \pm 1.5\,M_\odot\mathrm{yr}^{-1}$. The age of the stellar population for these SFHs is ~400 Myr, indicating that the bursts occur ~200 Myr prior to the time of observation. For the second run of FAST we additionally restricted the lower limit of the ages of the libraries used to fit the observed SED, such that a burst is implicitly forced to occur in these cases. We found that $\Delta t_{\mathrm{burst}} \geqslant 0.71$ Gyr models are not able to reproduce the observed SED well, hence we reject these scenarios as plausible SFHs for C1-23152. For the $\Delta t_{\mathrm{burst}} = 0.2$ Gyr and $\Delta t_{\mathrm{burst}} = 0.3$ Gyr models the best-fit stellar masses are $\log(M_*/M_\odot) = 11.46 \pm 0.03$ and $\log(M_*/M_\odot) = 11.51 \pm 0.03$, respectively. For both SFHs, the best-fit ages indicate that the bursts take place ~150–200 Myr prior to the epoch of observation, setting the formation redshifts to be $z_{\mathrm{form}} \sim 3.9$–$4.1$ for $\Delta t_{\mathrm{burst}} = 0.2$ Gyr and $z_{\mathrm{form}} \sim 4.1$–$4.5$ for $\Delta t_{\mathrm{burst}} = 0.3$ Gyr SFHs. Although the SED fits for the two-component SFHs systematically return higher χ^2 values compared to more simple exponentially declining or delayed SFHs, the best-fit stellar population parameters for $\Delta t_{\mathrm{burst}} \leqslant 0.3$ Gyr SFHs are consistent.

It is worth noting that the observed SED of C1-23152 bears a striking resemblance to the spectrum of Vega, an A0V star. It is plausible to assert that the SFH of C1-23152 is not composite as its age coincides with the time necessary for the turn-off point of main-sequence stars for a single stellar population to have almost reached AV0 stars. In this scenario the observed SED would be dominated by light from AV0 stars, explaining the similarity between the observed SED and spectrum of Vega. This serves as an additional constraint on the age and SFH of C1-23152.

3.3. Star Formation Rate from [O II]

We used the emission line [O II] λ3727 as an independent measure of the SFR and compared it to the values obtained from SED fitting. We emphasize that the [O II] detection is very marginal due to significant skyline contamination in the spectral region where the redshifted [O II] line falls. We used the L[O II]–SFR relation derived in Kewley et al. (2004) and obtained $\mathrm{SFR}([\mathrm{O\ II}]) = 30.9^{+42.1}_{-18.8}\ M_\odot\ \mathrm{yr}^{-1}$ (1σ error), larger by a factor of ~15 (for an exponentially declining SFH) and ~65 (for a delayed exponentially declining SFH) compared to the best-fit SFR values from the SED modeling. Studies find that radiation from LINER or Seyfert components in post-starburst and red sequence appears to be a more prominent source of [O II] line luminosity compared to star formation processes (Lemaux et al. 2010). Assuming that the [O III] line is purely of AGN origin in our spectra, we adopt an empirical relation between [O II] and [O III] to remove the component of the detected [O II] line that can be attributed to the presence of an AGN. Silverman et al. (2009) used the ratio [O II]/[O III] = 0.21 found in type 1 AGNs in the Sloan Digital Sky Survey (SDSS) sample with $\log L_{[\mathrm{O\ III}]} > 41.5$ to provide an estimate of the [O II] emission line luminosity free of any AGN contribution. We use this value to calculate an AGN-corrected upper limit to the SFR of the galaxy based on [O II] emission line luminosity and obtain $\mathrm{SFR}([\mathrm{O\ II}_{\mathrm{AGNcorrected}}]) = 17^{+44}_{-17}\ M_\odot\ \mathrm{yr}^{-1}$, consistent within the errors with the SFR derived from SED modeling. We note that while [O II]-derived SFR is very uncertain due to the large uncertainties in the [O II] line flux measurements, it is valuable as an independent tracer of the star formation rate.

3.4. Emission-line Properties: AGN versus Star Formation?

One diagnostic of AGNs in several studies has been the luminosity of the [O III] λ5007 optical nebular emission. We confirm that C1-23152's [O III] emission is indeed very luminous, $L_{[\mathrm{O\ III}]} = 1.65 \times 10^{43}\,\mathrm{erg\,s}^{-1}$. This value is at the high end of the range of [O III] luminosities found for Lyman break galaxies (LBG) and Lyα emitters at $z \simeq 2$–4 (e.g., Teplitz et al. 2000; Pettini et al. 2001; McLinden et al. 2011, and those harboring AGNs; Maschietto et al. 2008; Kuiper et al. 2011) and well above the [O III] luminosity the SED-derived SFRs would indicate.

At $z \gtrsim 3.3$, both [N II]λ6584 and Hα fall redward of the K band, i.e., at wavelengths where spectroscopy is not yet feasible. In the absence of both these nebular emission-lines, it is not possible to compare the line ratios of the galaxy on the

Table 3
Best-fit Stellar Population Parameters

	log (τ) (yr)	Metallicity	log (Age) (yr)	A_V (mag)	log (M_*) ($M_\odot$)	SFR ($M_\odot$ yr^{-1})	sSFR log(yr^{-1})	χ^2
SFH: Exponentially declining								
Free Z	$7.70^{+0.02}_{-0.30}$	$0.02^{+0.030}_{-0.003}$	$8.60^{+0.02}_{-0.23}$	$0.00^{+0.14}_{-0.00}$	$11.49^{+0.00}_{-0.09}$	$2.88^{+1.01}_{-2.28}$	$-11.03^{+0.20}_{-0.58}$	3.56
Free Z	$(7.00^{+0.40}_{-0.23})$	$(0.04^{+0.000}_{-0.006})$	$(8.30^{+0.03}_{-0.06})$	$(0.0^{+0.2}_{-0.0})$	$(11.41^{+0.05}_{-0.03})$	$(0.00^{+5.13}_{-0.00})$	$(-15.40^{+4.66}_{-4.54})$	(3.89)
$Z = 0.004$	$7.80^{+0.03}_{-1.30}$	0.004	$8.80^{+0.01}_{-0.10}$	$0.00^{+0.05}_{-0.00}$	$11.56^{+0.00}_{-0.05}$	$0.37^{+0.00}_{-0.37}$	$-11.99^{+0.00}_{-87.01}$	3.86
$Z = 0.008$	$7.70^{+0.10}_{-1.20}$	0.008	$8.70^{+0.01}_{-0.12}$	$0.00^{+0.12}_{-0.00}$	$11.54^{+0.00}_{-0.07}$	$0.44^{+1.91}_{-0.44}$	$-11.90^{+0.78}_{-87.10}$	3.80
$Z = 0.02$	$7.70^{+0.02}_{-0.64}$	0.02	$8.60^{+0.01}_{-0.10}$	$0.00^{+0.09}_{-0.00}$	$11.49^{+0.00}_{-0.06}$	$2.88^{+0.00}_{-2.88}$	$-11.03^{+0.00}_{-6.57}$	3.52
$Z = 0.05$	$7.50^{+0.00}_{-0.10}$	0.05	$8.40^{+0.00}_{-0.03}$	$0.10^{+0.04}_{-0.10}$	$11.42^{+0.00}_{-0.02}$	$3.89^{+0.00}_{-3.29}$	$-10.83^{+0.00}_{-0.78}$	3.52
SFH: Delayed exponentially declining								
Free Z	$7.60^{+0.15}_{-1.10}$	$0.008^{+0.042}_{-0.004}$	$8.70^{+0.14}_{-0.33}$	$0.00^{+0.13}_{-0.00}$	$11.49^{+0.06}_{-0.08}$	$0.48^{+4.65}_{-0.48}$	$-11.81^{+1.09}_{-87.19}$	3.63
Free Z	$(6.70^{+0.70}_{-0.20})$	$(0.04^{+0.000}_{-0.015})$	$(8.30^{+0.10}_{-0.14})$	$(0.00^{+0.42}_{-0.00})$	$(11.41^{+0.11}_{-0.02})$	$(0.00^{+6.76}_{-0.00})$	$(-21.55^{+10.92}_{-8.78})$	(3.92)
$Z = 0.004$	$7.60^{+0.10}_{-0.05}$	0.004	$8.80^{+0.02}_{-0.05}$	$0.00^{+0.03}_{-0.00}$	$11.55^{+0.00}_{-0.03}$	$0.03^{+0.4}_{-0.00}$	$-13.08^{+1.17}_{-0.00}$	3.63
$Z = 0.008$	$7.60^{+0.20}_{-1.10}$	0.008	$8.70^{+0.10}_{-0.13}$	$0.00^{+0.16}_{-0.00}$	$11.49^{+0.07}_{-0.03}$	$0.48^{+3.07}_{-0.48}$	$-11.81^{+0.80}_{-87.19}$	3.59
$Z = 0.02$	$7.50^{+0.10}_{-0.99}$	0.02	$8.60^{+0.02}_{-0.17}$	$0.00^{+0.18}_{-0.00}$	$11.48^{+0.00}_{-0.06}$	$0.58^{+4.10}_{-0.58}$	$-11.72^{+0.90}_{-25.02}$	3.71
$Z = 0.05$	$7.30^{+0.20}_{-0.77}$	0.05	$8.40^{+0.10}_{-0.14}$	$0.10^{+0.22}_{-0.10}$	$11.41^{+0.03}_{-0.03}$	$0.51^{+3.75}_{-0.51}$	$-11.52^{+0.80}_{-13.89}$	3.76
SFH: Truncated								
Free Z	$8.20^{+0.43}_{-1.70}$	$0.008^{+0.042}_{-0.004}$	$8.70^{+0.23}_{-0.46}$	$0.00^{+0.33}_{-0.00}$	$11.50^{+0.08}_{-0.12}$	0	–99	3.62
	$(7.40^{+0.93}_{-0.90})$	$(0.04^{+0.000}_{-0.039})$	$(8.30^{+0.17}_{-1.30})$	$(0.00^{+2.50}_{-0.00})$	$(11.41^{+0.12}_{-0.04})$	(0)	(-99)	(4.54)
AGN continuum subtracted; SFH: Exponentially declining								
$\alpha \sim 1.6$								
Free Z	$7.70^{+0.82}_{-1.20}$	$0.02^{+0.03}_{-0.013}$	$8.60^{+0.14}_{-0.3}$	$0.00^{+0.10}_{-0.00}$	$11.44^{+0.14}_{-0.01}$	$2.57^{+0.00}_{-2.57}$	$-11.03^{+0.00}_{-99}$	4.43
Mrk231 template								
Free Z	$7.70^{+0.05}_{-1.20}$	$0.02^{+0.03}_{-0.009}$	$8.60^{+0.08}_{-0.34}$	$0.00^{+0.25}_{-0.00}$	$11.46^{+0.00}_{-0.14}$	$2.69^{+0.94}_{-0.00}$	$-11.03^{+0.20}_{-21.05}$	4.52
DR2 template								
Free Z	$7.50^{+0.10}_{-1.00}$	$0.02^{+0.03}_{-0.005}$	$8.60^{+0.04}_{-0.21}$	$0.00^{+0.07}_{-0.00}$	$11.49^{+0.01}_{-0.11}$	$0.05^{+0.41}_{-0.05}$	$-12.80^{+0.99}_{-25.70}$	8.03
TQSO1 template								
Free Z	$6.90^{+0.73}_{-0.40}$	$0.05^{+0.00}_{-0.038}$	$8.40^{+0.27}_{-0.04}$	$0.00^{+0.02}_{-0.00}$	$11.39^{+0.11}_{-0.01}$	$0.00^{+0.46}_{-0.00}$	$-20.03^{+8.22}_{-18.47}$	7.91

Notes. Estimated stellar population parameters from the modeling of the binned UV-to-NIR spectra in combination with the broad- and medium-bandwidth photometry from NMBS. The values in parentheses correspond to the best-fit stellar population parameters assuming the Maraston (2005) SPS models, while the values not in parentheses correspond to the best-fit parameters derived assuming the Bruzual & Charlot (2003) stellar population synthesis models. Quoted errors are 3σ confidence intervals output by FAST (see Kriek et al. 2009 for a detailed description of the adopted method in FAST to estimate confidence intervals). A Kroupa (2001) IMF and a Calzetti et al. (2000) extinction law are assumed in all cases.

most widely used emission-line diagnostic, the BPT diagram (Baldwin et al. 1981), which employs optical nebular line ratios of [N II]/Hα and [O III]/H β to distinguish star-forming galaxies, Seyfert 2 galaxies (or AGN NLRs), and LINER galaxies.

Recently, Juneau et al. (2011, 2014) introduced a new excitation diagnostic that could be used in the absence of [N II] and Hα measurements, namely, the Mass-Excitation diagnostic (MEx). This diagnostic uses the well-known correlation between galaxy stellar mass and gas-phase metallicity (Tremonti et al. 2004) to create an alternate BPT-like diagram with [O III]/H β versus stellar mass. We determine a lower limit to [O III]/H β ratio by assuming that Hβ has the same width as [O III] and a peak flux three times the rms measured in the same spectral region, implying log ([O III]/Hβ) $\geqslant$ 1.27. Given the stellar mass derived from SED modeling, i.e., log ($M_*/M_\odot$) = 11.49, the estimated lower limit on log ([O III]/Hβ) implies the presence of an AGN in C1-23152, based on its position on the MEx diagnostic diagram. We also note that the estimated lower limit on log ([O III]/Hβ) is a factor of ~4 larger compared to the unusually high mean [O III]/H β ratio found by Holden et al. (2014) in a sample of LBGs at $z \sim 3.5$ with log ($M_*/M_\odot$) < 10.5 and significantly larger specific SFR (e.g., log(sSFR/yr^{-1}) > $-$ 9) compared to C1-23152.

The large values for the line ratio of [O III]/Hβ are inconsistent with stellar photoionization and indicative of photoionization by an AGN. The AGN interpretation is further confirmed by the comparably weak [O II] emission, such that the [O III]/[O II] ratio $\sim 2.2^{+3.6}_{-1.7}$ (measured assuming identical widths and redshift for both lines). This line ratio is a sensitive diagnostic of the ionization parameter and efficiently separates Seyfert-like objects from star-forming galaxies and LINERs at low redshift (Kewley et al. 2006). Because we lack any constraints on [O I]/Hα that could further help separate the AGN from star-forming and composite galaxies, at [O III]/[O II] >1 the main ambiguity is between Seyferts and low-metallicity galaxies with significant ongoing star formation (Dopita

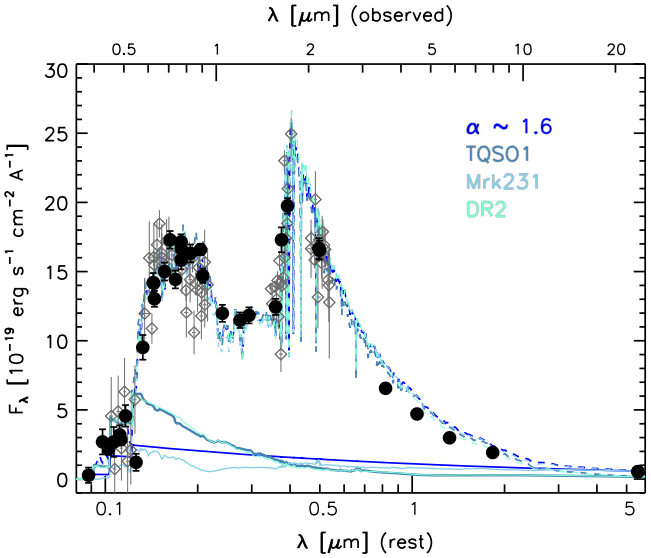

Figure 4. Observed SED of C1-23152 from the U band to the MIPS 24 μm; filled black circles represent the broad- and medium-band photometry, while the gray open diamonds show the binned spectra. The continuous curves show the four AGN templates with their maximum contributions constrained by the observed 24 μm flux and/or the rest-frame UV flux. The dashed curves show the combinations of the AGN templates and the best-fit FAST models obtained when fitting the AGN-continuum-corrected SED of C1-23152. The different colors represent the four adopted AGN templates. Templates for Mrk 231, TQSO1, and DR2 are from Polletta et al. (2007) and Salvato et al. (2009): TQSO1 and DR2 represent high IR luminosity and low-luminosity QSO templates, respectively, with a power-law component extended into the UV.

et al. 2006; Nakajima et al. 2013). The upper limit on SFR obtained from [O II] line luminosity along with the small values of SFRs from the SED modeling provides strong evidence that the galaxy is not a starbursting galaxy. The evaluation of C1-23152 using the MEx diagnostic further supports the AGN-like nature of the line emissions.

3.5. Continuum Emission from the AGN

In the previous sections, we found that C1-23152 likely hosts a luminous AGN from emission-line properties. The AGN continuum emission could potentially contribute to the observed SED, biasing the derived stellar population parameters. We investigated this by subtracting the AGN contribution from the observed SED and by re-fitting the corrected SED. Specifically, we assumed a power-law SED for the AGN, with $F_\nu \propto \nu^\alpha$. The value of α was derived by fitting the rest-frame UV and the MIPS 24 μm photometry and spectroscopy for maximal AGN SED contribution, corresponding to $\alpha \sim -1.6$. The maximum AGN contribution is then set by the rest-frame UV fluxes in combination with the 24 μm band and subtracted from the observed SED. The resulting SED is finally remodeled using FAST to derive stellar population parameters (listed in Table 3). We find that the derived stellar mass is smaller by $\sim$0.05 dex, resulting in $\log(M_*/M_\odot) = 11.44$ (i.e., $M_* \approx 2.8 \times 10^{11} M_\odot$).

We also used QSO templates from Polletta et al. (2007) and Salvato et al. (2009) to fit the maximum AGN continuum contribution in a similar manner as above to constrain the stellar population parameters of the galaxy. The templates used include the heavily obscured broad absorption line QSO, Mrk 231, and optically selected QSO with different IR to optical flux ratios. The AGN-continuum-subtracted SEDs were remodeled using FAST with a Kroupa IMF, exponentially declining SFH and BC03 SPS models, and the best-fit stellar properties are listed in Table 3. Figure 4 shows the observed SED of C1-23152 from the U band to the MIPS 24 μm overplotted on the adopted AGN templates with their maximum contributions constrained by the observed SED. Also plotted are the combinations of the best-fit FAST models of the AGN-continuum subtracted SED and the adopted AGN templates. The best-fit stellar population parameters are again consistent with zero dust attenuation and low SFR; the stellar mass of the galaxy is lower on average by $\sim$0.05 dex, compared to best-fit values modeled using the observed SED. The minimum stellar mass allowed by the 3σ uncertainties is $\log(M_*/M_\odot) = 11.32$ (i.e., $M_* \approx 2.1 \times 10^{11} M_\odot$), confirming that the observed SED of the galaxy is dominated by the stellar light, rather than the AGN emission, and confirming the very large stellar mass of C1-23152.

3.6. Further Evidence for Hidden Luminous Quasar

3.6.1. AGN Luminosity

The AGN-like line ratios and line widths suggest that C1-23152 hosts a luminous AGN. If we ignore the contribution from strong ionizing radiation fields due to star formation, we can use the [O III] luminosity as a direct proxy for the bolometric luminosity of the quasar. We used the bolometric correction ($C_{[\mathrm{O\,III}]}$) for extinction-corrected $L_{[\mathrm{O\,III}]}$ derived by Lamastra et al. (2009) $L_{\mathrm{bol,AGN}} \approx 454\, L_{[\mathrm{O\,III}]}$ for extinction-corrected [O III] luminosities to find $L_{\mathrm{bol}} = 7.5^{+5.9}_{-3.3} \times 10^{45}$ erg s^{-1}. The authors in this study use a sample of type-2 AGNs in SDSS with reliable $L_{[\mathrm{O\,III}]}$ and X-ray luminosities (L_{X}) to estimate $C_{[\mathrm{O\,III}]}$ combining the observed correlation between $L_{[\mathrm{O\,III}]}$ and L_{X} with the X-ray bolometric correction (Marconi et al. 2004). We also estimated the ionizing luminosity, L_{ion}, from the total luminosity in narrow lines, L_{NLR}. Using $L_{\mathrm{NLR}} = 3(3L_{[\mathrm{O\,II}]} + 1.5L_{[\mathrm{O\,III}]})$ and $L_{\mathrm{ion}} = L_{\mathrm{NLR}} \times C^{-1}$ and adopting a covering factor of $C \sim 10^{-2}$ (Rawlings & Saunders 1991), we find $L_{\mathrm{ion}} = 14.2^{+6.6}_{-4.5} \times 10^{45}$ ergs^{-1}. Both estimates imply the presence of a luminous hidden quasar.

3.6.2. Infrared Spectral Energy Distribution

Figure 5 shows the observed far-infrared (FIR) SED of C1-23152, including fluxes in the *Spitzer*-MIPS 24 μm (from the NMBS catalog of Whitaker et al. 2011), *Herschel*-PACS 100, 160 μm and SPIRE 250, 350, 500 μm, the 2 mm Goddard-IRAM Superconducting 2 Millimeter Observer (GISMO) on the IRAM 30 m telescope (A. Karim et al. 2015, in preparation), and the 320 MHz data from the Giant Meterwave Radio Telescope (A. Karim et al. 2015, in preparation). The PACS and SPIRE photometry was extracted from the images of the PACS Evolutionary Probe survey (Lutz et al. 2011), the Herschel Multi-tiered Extragalactic Survey (HerMES; Oliver et al. 2012), and Herschel-CANDELS (PI: Dickinson) as described in A. P. G. B. Bedregal et al. (2015, in preparation). The 1σ detection limits of *Herschel* photometry are 1.7 and 3.4 mJy for PACS 100 μm (Berti et al. 2011), 160 μm and 3.2, 2.7, 3.8 mJy for SPIRE 250, 350, 500 μm photometry (Oliver et al. 2012), respectively. The source is not robustly detected ($>3\sigma$) in any of the FIR bands, except in the MIPS 24 μm ($\sim 7\sigma$); the SPIRE fluxes have an S/N $\lesssim$2. The source is also

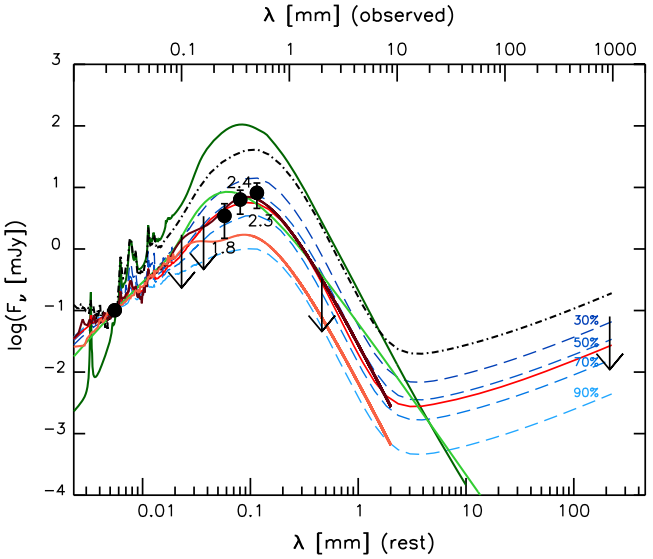

Figure 5. IR SED with *Spitzer* MIPS 24 μm, *Herschel* PACS 100 μm, 160 μm, SPIRE 250, 350, 500 μm, GISMO 2 mm and 320 MHz data from GMRT with IR templates fit to 24 μm photometry overplotted. Filled black circles represent observations with detections above 1σ with the significance of detection indicated by the S/N at each point. Photometric points with no detection are indicated as 1σ upper limits. Light green solid template represents the best-fit obtained using the FIR blackbody models from Casey (2012); dark green solid template represents the starburst SED from Magdis et al. (2012); high-z composite AGN templates with and without silicate features from Kirkpatrick et al. (2012) are plotted in dark red and orange triple-dot dashed lines respectively; dashed (blue) templates represent the mean SEDs for $\alpha = 1, \ldots, 2.5$ from the template set of Dale et al. (2014) for varying degrees of AGN contribution (dark blue: 0% to light blue: 100% AGN contribution in uniform 20% steps); red solid SED is the template from Dale et al. (2014) that minimizes χ^2 and black dot dashed SED represents the average SED of Dale & Helou (2002) templates used in Marchesini et al. (2010). IR templates with only obscured star formation cannot model the full observed IR SED; an AGN contribution of >50% is required to reproduce the observed IR SED.

not detected in the Submillimeter Common User Bolometric Array-2 (SCUBA-2; Holland et al. 2013) deep 450 μm and 850 μm observations on the James Clerk Maxwell Telescope (JCMT) Casey et al. (2013), or in 1.1 mm AzTEC Surveys (Scott et al. 2008; Aretxaga et al. 2011).

The observed 24 μm band probes the rest-frame ~5.5 μm, corresponding to the spectral region of thermal emission from hot dust at the redshift of C1-23152. The source of the mid-infrared (MIR) emission was investigated by Marchesini et al. (2010). Assuming that all the luminosity at the observed 24 μm is associated with dust-enshrouded star formation, Marchesini et al. (2010) adopted the mean of $\log L_{\mathrm{IR},\alpha=1,\ldots,2.5}$ from the template set of Dale & Helou (2002) (presented in Figure 5 as a dot-dashed black curve) to estimate a total 8–1000 μm rest-frame IR luminosity $L_{\mathrm{IR}} = 1.14 \times 10^{13}\, L_{\odot}$, corresponding to an SFR $\sim 1260\, M_{\odot}\ \mathrm{yr}^{-1}$ when using the L_{IR}-SFR calibration adapted for a Kroupa (2001) IMF from Kennicutt (1998). Larger values of L_{IR} and SFR would be estimated if using the starburst template from Magdis et al. (2012; dark green curve in Figure 5). In place of the Dale & Helou (2002) templates, we also use the calibration by Rujopakarn et al. (2013) to obtain $L_{\mathrm{IR}} = 7.45 \times 10^{12}\ L_{\odot}$ and SFR $\sim 835\, M_{\odot}\ \mathrm{yr}^{-1}$. An independent estimate of L_{IR} can be finally derived from the IDL code of Casey (2012) to fit a modified blackbody to the FIR detections and upper limits, resulting in $L_{\mathrm{IR}} = 4.34 \times 10^{12}$ $L_{\odot}$ and SFR $\sim 480\, M_{\odot}\ \mathrm{yr}^{-1}$ (the light green SED in Figure 5 represents this best-fit model). All of these values of SFR are from many hundreds to a couple of thousands times larger than the SFRs estimated from SED modeling, and a factor of ~30–45 larger than the SFR derived using the AGN-corrected [O II] line luminosity.

The inconsistency of the 24 μm-derived SFR, which assumes that the MIR emission originates from dust-enshrouded star formation, compared to the SED- and [O II]-derived SFRs provides further evidence that C1-23152 hosts a powerful AGN. Moreover, as shown in Figure 5, no model in which the IR emission is due only to obscured star formation can reproduce the observed IR SED. Indeed, significant contributions from an obscured AGN are required to match the observations. We use the IR template set of Dale et al. (2014), which includes fractional AGN contributions to IR radiation to investigate constraints on the source of radiation responsible for FIR detections. For visual ease in comparison, we calculate the mean $\log L_{\mathrm{IR}}$ for $\alpha = 1, \ldots, 2.5$ from this template set for AGN contributions of 30%, 50%, 70%, and 90%, scaled to the observed MIPS 24 μm photometry. These mean templates are plotted as blue dashed lines in Figure 5 with the contribution of AGN in 20% increments. We fit the detections and the upper limits with the individual templates from Dale et al. (2014). The template with 60% AGN contribution and $\alpha = 1.6875$ yields the minimum χ^2 and is shown in Figure 5 as a red solid curve. The IR detections and 1σ upper limits effectively rule out dust-enshrouded star formation as the only source of the observed 24μm flux, with the AGN contributing >60% to the IR SED of C1-23152.

To estimate the bolometric luminosity of the quasar independently of emission-line luminosities, we used the two high-z composite templates of AGNs from Kirkpatrick et al. (2012), one with a clear 9.7 μm silicate absorption feature and the other with a featureless MIR spectrum. We scaled the AGN templates from Kirkpatrick et al. (2012) (plotted in Figure 5 in dark red and orange triple-dot dashed curves for the templates with and without silicate features, respectively) to the observed 24 μm (rest-frame 5.5 μm) luminosity of C1-23152.

Using the integrated luminosities of the SED templates, we find $L_{\mathrm{bol,AGN}} \approx (8.9 \pm 2.7) \times 10^{45}\ \mathrm{erg\ s}^{-1}$ and $L_{\mathrm{bol,AGN}} \approx (15.2 \pm 6.5) \times 10^{45}\ \mathrm{erg\ s}^{-1}$ for the featureless AGN template and the AGN template with silicate absorption, respectively, in good agreement with the bolometric AGN luminosities estimated from the emission-line luminosities.

3.6.3. Radio/X-Ray Emission

We have used the publicly available *Chandra* X-ray data available over the COSMOS field (Elvis 2009) to search for X-ray detection. C1-23152 is not detected. Using the 3σ detection flux limits, we derived the 3σ upper limit to the rest-frame 2–10 keV luminosity of $L_{2-10\,\mathrm{keV}} \approx 1.9 \times 10^{44}\ \mathrm{erg\ s}^{-1}$, assuming a power-law photon index of $\Gamma = 1.9$ (Nandra & Pounds 1994).

To investigate whether the expected X-ray flux of C1-23152 is below this detection limit, we used two methods to calculate the expected X-ray luminosity. We first employed the relation between MIR (12 μm) and X-ray luminosities observed by Gandhi et al. (2009) in local Seyferts, assuming the two high-z AGN SEDs as above. We found $L_{2-10\,\mathrm{keV}} \approx (9.0 \pm 3.5) \times 10^{44}\ \mathrm{erg\ s}^{-1}$ and $\approx (9.1 \pm 3.6) \times 10^{44}\ \mathrm{erg\ s}^{-1}$ for the featureless and silicate AGN templates, respectively.

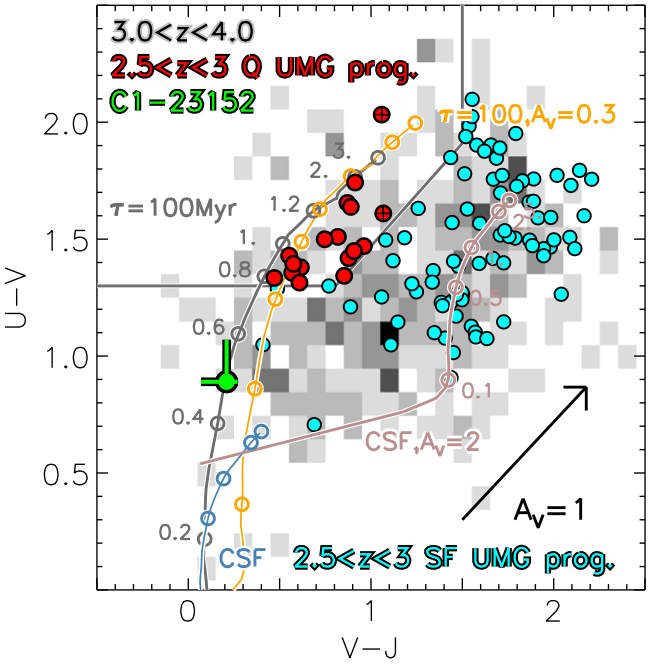

Figure 6. Rest-frame $U - V$ vs. $V - J$ color–color diagram. The grayscale representation indicates the distributions of all galaxies with $M_\star > 5 \times 10^{10}\,M_\odot$ at $3.0 \leqslant z \leqslant 4.0$ from the K_s-selected UltraVISTA catalog (Muzzin et al. 2013a). The cuts used to separate star-forming from quiescent galaxies from Muzzin et al. (2013b) are shown as the solid dark gray lines. The green point indicates the color for C1-23152, with error bars representing the total 1σ uncertainties. Red filled points and blue filled points are the quiescent and star-forming progenitors, respectively, of local UMGs at $2.5 < z < 3.0$ from Marchesini et al. (2014), with crosses indicating sources with MIPS detection at $\geqslant 5\,\sigma$. Color evolution tracks of Bruzual & Charlot (2003) models are also shown: an exponentially declining SFH with no dust ($\tau = 100$ Myr; gray), the same exponentially declining SFH with $A_V = 0.3$ mag ($\tau = 100$ Myr; orange), a constant SFH with no dust (CSF; light blue), and the same CSF model with $A_V = 2$ mag of extinction (light brown). The empty circles represent the model colors at the specified ages (in Gyr). The dust vector indicates an extinction of $A_V = 1$ mag for a Calzetti et al. (2000) extinction curve.

We also estimated the rest-frame $L_{2-10\,\mathrm{keV}}$ luminosity using the bolometric correction adopted from Hopkins et al. (2007) again using the same two AGN SED templates as above. The resulting X-ray luminosities are $L_{2-10\,\mathrm{keV}} \approx (1.6 \pm 0.5) \times 10^{44}$ erg s^{-1} and $\approx (2.4 \pm 1.1) \times 10^{44}$ erg s^{-1} for the silicate absorption and the featureless templates, respectively. The estimated X-ray luminosities using the Gandhi et al. (2009) relation imply that the non-detection of C1-23152 in the X-rays would require a Compton-thick nature of the AGN, whereas the X-ray luminosities estimated using the bolometric correction from Hopkins et al. (2007) can be compatible with the observational flux limitations. We stress that these calibrations are based on low-redshift samples and the large uncertainties associated in both estimates prohibit us from making firmer conclusions about the X-ray properties of C1-23152.

C1-23152 is also not detected in the publicly available 1.4 GHz VLA radio data available over the COSMOS field (Schinnerer et al. 2010). The 3σ limit for the intrinsic $L_{1.4\,\mathrm{GHz}}$ at the redshift of our target is sufficient to rule out a radio-loud AGN (i.e., $\log(L_{1.4\,\mathrm{GHz}}[W\ \mathrm{Hz}^{-1}]) < 25$; Schinnerer et al. 2007), but does not provide any meaningful SFR estimates. Given the numerous evidence for the (almost) post-starburst state of C1-23152, a non-detection is not surprising, as radio-loud AGNs are commonly found in hosts with SFR $\sim 300\ M_\odot\ \mathrm{yr}^{-1}$ at $z \sim 2$ (Floyd et al. 2013).

3.7. UVJ Colors

The rest-frame $U - V$ versus $V - J$ diagram (hereafter, UVJ diagram) has become a popular way to differentiate between star-forming and quiescent galaxies, with galaxy populations clearly separated in this color–color space (Labbé et al. 2005; Wuyts et al. 2007; Williams et al. 2009; Brammer et al. 2011; Whitaker et al. 2011; Patel et al. 2012, 2013; Muzzin et al. 2013b). Figure 6 shows the rest-frame $U - V$ and $V - J$ colors of C1-23152 (green) overplotted to the distribution in the UVJ diagram of all galaxies at $3.0 < z < 4.0$ from the K_S-selected UltraVISTA catalog of Muzzin et al. (2013a) (grayscale representation). We calculated the rest frame $U - V$ and $V - J$ colors of C1-23152 using EAZY (Brammer et al. 2008). A Monte Carlo approach was used to measure the uncertainties in the $U - V$ and $V - J$ colors. Specifically, 1000 photometry catalogs were created by perturbing each flux by a Gaussian random number with the standard deviation set by the level of each flux error. The simulated catalogs were each fit with EAZY separately, and the formal upper and lower limits were obtained in a similar manner as for the emission-line fits.

The colors of C1-23152, $U - V = 0.89^{+0.18}_{-0.02}$ mag and $V - J = 0.21^{+0.06}_{-0.14}$ mag, place it formally outside the commonly defined quiescent region, with a $U - V$ color intermediate between a star-forming galaxy with no dust and a quiescent post-starburst galaxy. Figure 6 also shows color–color evolution tracks for different SFHs and dust extinction. The gray and orange tracks represent the evolution of an exponentially declining SFH with $\tau = 100$ Myr and $A_V = 0$ and 0.3 mag, respectively. The blue and light brown tracks represent the color evolution of constant star formation history with $A_V = 0$ and 2.0 mag, respectively. Figure 6 shows that the derived $U - V$ and $V - J$ colors of C1-23152 match the colors predicted for a stellar population characterized by an exponentially declining SFH with $\tau = 100$ Myr, no dust extinction, and an age of $\approx$0.5 Gyr, consistent within the errors with the stellar population properties of C1-23152 derived from the SED modeling.

As described in Section 3.2, we performed SED fits for composite SFHs that include an old and young population. We used the best-fit parameters obtained for the composite SFH to investigate the rest-frame $U - V$ and $V - J$ colors of the underlying old population. For the two-component SFH models that reproduce the observed SED reasonably well, we found that the rest-frame $U - V$ and $V - J$ colors of the old stellar population are only slightly redder, $\langle \Delta(U - V) \rangle = \langle \Delta(V - J) \rangle \sim 0.3$ mag. This is expected as by construction, composite SFHs will result in the old stellar component to be slightly more evolved compared to stellar populations obtained from simple SFHs. Nevertheless, the colors obtained of the old stellar components for these SFHs are still similar to those derived assuming an exponentially declining SFH and are typical of a galaxy in a post-starburst phase about to enter the quiescent box. We therefore conclude that the influence of a recent burst does not change the overall interpretation of the color evolution of C1-23152.

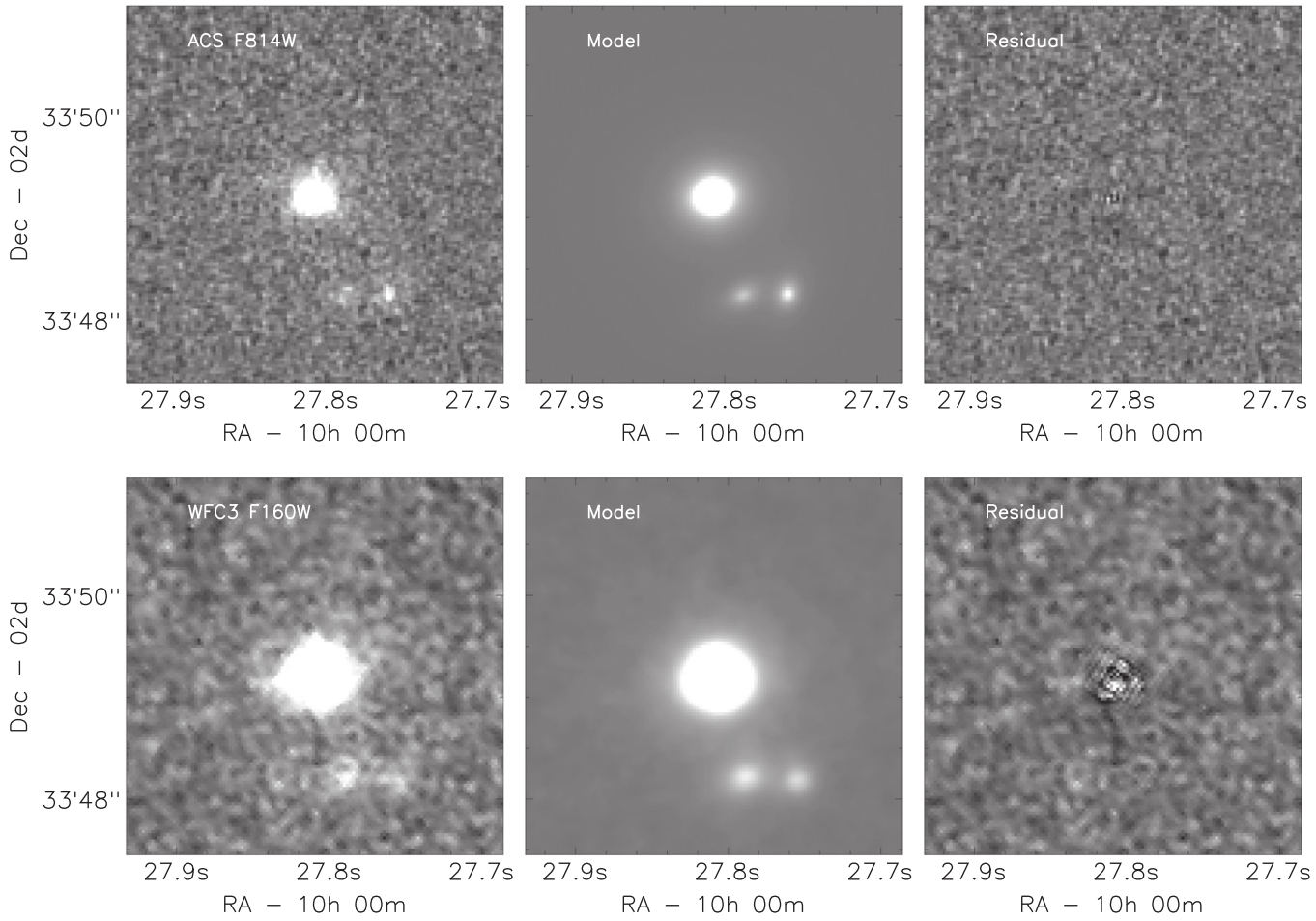

Figure 7. Left column: ACS (top) and WFC3 (bottom) images for C1-23152. The galaxy is resolved in both bands. Central column: best-fit GALFIT modeling. Right column: residual images. The best-fit GALFIT values are $r_{e,circ} = 1.45 \pm 0.15$ kpc, $n = 5.5 \pm 0.5$ and $b/a = 0.85 \pm 0.04$ for ACS imaging, and $r_{e,circ} = 0.97 \pm 0.10$ kpc, $n = 4.4 \pm 0.4$ and $b/a = 0.82 \pm 0.03$ for WF3 imaging. C1-23152 is more compact (by ∼50%) in H_{160} (rest-frame *U*-band) than in the ACS I_{814} (rest-frame UV). There is no evidence for a central point-like source in either band.

3.8. Size

We used ACS I_{814} and *HST* F 160*W* imaging to measure the structural parameters of the galaxy probing the rest-frame UV ($\lambda_{rest} \approx 1870$ Å) and the rest-frame optical ($\lambda_{rest} \approx 3680$ Å), respectively. Structural parameters were obtained with GALFIT (Peng et al. 2002), which provides measurements of the Sérsic index (n), effective radius (r_e), and axis ratio (b/a). Visual inspection of the *HST* images showed that C1-23152 is accompanied by two fainter objects $\lesssim 2''$ southwest of its center. Although much fainter than C1-23152 (by ∼2.5 and 3.6 mag in the H_{160} band, and ∼2.6 mag in the I_{814} band), these two objects could contaminate the light profile of C1-23152, potentially introducing systematic effects in the recovery of the structural parameters. The measurements were therefore performed fitting the light profiles of the three sources simultaneously.

For each object, a single Sérsic profile was considered. The effective radius was circularized following the relation $r_{e,circ} = r_e\sqrt{b/a}$. The point-spread function (PSF) in each *HST* band was built from a sample of bright and isolated point sources and combined together with the IRAF task `daophot/psf`. The PSF FWHM for the ACS I_{814} is 0.″1 and 0.″17 for the WFC3 H_{160} band. The values recovered for the circularized effective radius are $r_{e,circ} = 0.''195 \pm 0.''021$ and $r_{e,circ} = 0.''130 \pm 0.''013$ for the ACS I_{814} and the WFC3 H_{160} bands, respectively. The estimated values of the Sérsic index and the axis ratios are $n = 5.5 \pm 0.5$ and $n = 4.4 \pm 0.4$, and $b/a = 0.85 \pm 0.04$ and $b/a = 0.82 \pm 0.03$ for the I_{814} and the H_{160} bands, respectively. Figure 7 shows, for each band, a cutout from the original frame centered on C1-23152, the GALFIT model, and the residual image after subtracting the model from the original frame. As a consistency check, we also run GALFIT masking the two neighboring sources and verifying that the morphological parameters obtained in this way did not differ sensibly from those obtained including the two neighboring sources. Figure 8 shows a color image obtained from the combination of the I_{814} and H_{160} bands of a cutout centered around C1-23152. Whereas C1-23152 shows a smooth and round morphology, with no obvious radial color gradient, the two nearby fainter sources are clearly bluer.

Observationally, an AGN could manifest itself as a brighter point source in the central region of the galaxy. Visual inspection of the residual images from the Sérsic profile fitting process did not show any evident sign of a residual point source. However, its existence was also tested by including a point-source component and re-running GALFIT. The resulting flux in each band was a value consistent with no flux, causing GALFIT to crash, and confirming the result from visual inspection. We finally re-run GALFIT by fixing the magnitude

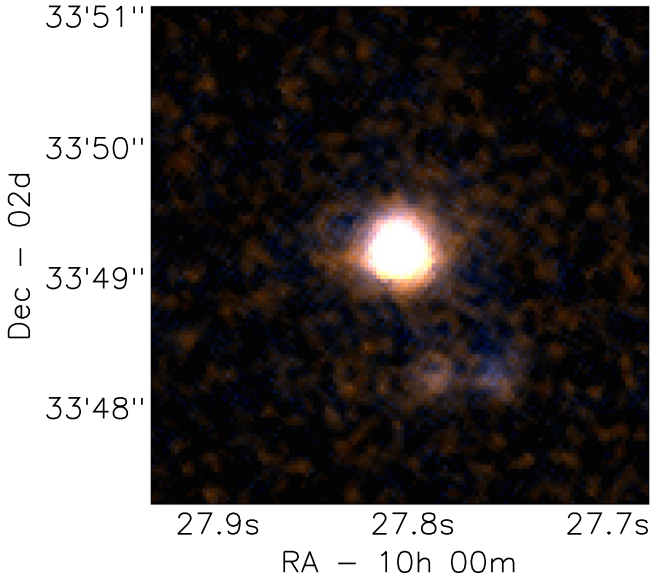

Figure 8. Color image obtained from the combination of the *HST* ACS I_{814} and WFC3 H_{160} bands centered around C1-23152. C1-23152 shows a smooth and round morphology; the two nearby fainter sources are characterized by bluer colors.

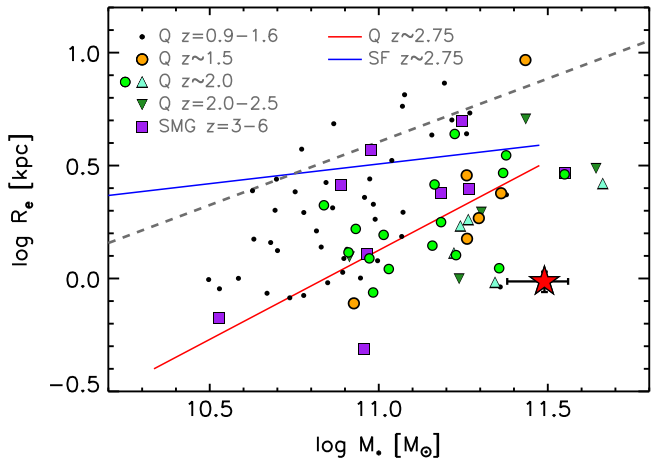

Figure 9. Plot of stellar mass versus size. Red star indicates the location of C1-23152. Spectroscopically confirmed quenched galaxies are indicated in the legend with Q and the redshift range of each study (black points: Belli et al. 2014a; orange filled circles: Bezanson et al. 2013; green filled circles: Krogager et al. 2013; light blue triangles: van De Sande et al. 2013; dark green downward triangles: Belli et al. 2014b). Purple filled squares indicate the location of spectroscopically confirmed SMGs from Toft et al. (2014). Red and blue solid lines indicate the median mass versus size distribution for quiescent and star-forming galaxies, respectively, from van der Wel et al. (2014). Dark gray dashed line is the mean stellar mass versus size at $z \sim 0$ from Shen et al. (2003). All measurements are scaled to match a Kroupa (2001) IMF.

of the central point-source component to the values obtained from the maximized AGN contributions derived in Section 3.5. The contributions of the AGN to the total fluxes in the H_{160} and I_{814} bands are ∼8–15% and ∼9–29%, respectively, depending on the AGN template. Fixing the magnitude of the central point-source component results in slightly larger effective radii, consistent within 2σ with the values obtained without a central point-source component. Specifically, we obtained $r_{e,circ} = 0\farcs20 - 0\farcs23$ and $r_{e,circ} = 0\farcs14 - 0\farcs16$ for the ACS I_{814} and the WFC3 H_{160} bands, respectively, depending on the adopted AGN contribution. Whereas the effective radius does not change significantly when including a central point source, the Sérsic index is much more sensitive, and ranges in $n = 0.7$–3.9 and $n = 3.0$–3.6 for the ACS I_{814} and the WFC3 H_{160} bands, respectively, depending on the adopted AGN contribution. We note, however, that the inclusion of the central point-source component results in increasingly worse modeling of the *HST* images for increasing AGN contributions, especially for the I_{814} band, and that significant positive and negative features appear in the center of the galaxy on the residual images output by GALFIT, indicative of oversubtraction of the central point-like component.

Figure 9 shows the stellar mass versus size diagram of spectroscopically confirmed quenched galaxies at $z < 3$ (Bezanson et al. 2013; Krogager et al. 2013; van De Sande et al. 2013; Belli et al. 2014a, 2014b) and spectroscopically confirmed SMGs (Toft et al. 2014), along with the stellar mass and size of C1-23152, highlighting the extreme compactness of this galaxy. At the redshift of the source, $z_{spec} = 3.351$, the measured circularized effective radii correspond to linear sizes of $r_{e,circ} = 1.45 \pm 0.15$ kpc in the I_{814} and $r_{e,circ} = 0.97 \pm 0.1$ kpc in the H_{160} band.[14] Interestingly, the effective radius in the rest-frame optical is smaller that the effective radius in the rest-frame UV by $\sim 0.5 \pm 0.2$ kpc, with a gradient $\Delta \log r_{eff}/\Delta \log \lambda = -0.13 \pm 0.07$, broadly consistent with $\Delta \log r_{eff}/\Delta \log \lambda = -0.25$ in a sample of early-type galaxies at $0 < z < 2$ found by van der Wel et al. (2014). If we consider the circularized effective radius of ∼1 kpc derived from the H_{160} band, C1-23152 is a very compact galaxy for its large stellar mass, arguably among the most compact very massive galaxies at $z > 3$ (see Figure 9). More quantitatively, the size of C1-23152 is a factor of ∼2 smaller than the median size of galaxies at $2.5 < z < 3.0$ with similar stellar masses ($11 < \log M_*/M_\odot < 11.5$), and it is consistent with the 16% range in the size distribution of this sample (van der Wel et al. 2014). We finally note that C1-23152 is best modeled by a Sérsic index $n = 4.4 \pm 0.4$ in the H_{160} band, consistent with a de Vaucouleur's profile ($n = 4$), and a large axis ratio of $b/a \sim 0.8 - 0.9$. The best-fit structural and stellar population parameters for C1-23152 are in line with other studies of early-type galaxies at $z > 1$ (Franx et al. 2008; van Dokkum et al. 2011; Wuyts et al. 2011; Wake et al. 2012; Bell et al. 2012; Chang et al. 2013) that have shown that sources with high Sérsic indices and large axis ratios are more likely to be quiescent.

4. SUMMARY AND DISCUSSION

In this paper we have investigated the extensive (observed-frame) UV-to-NIR spectra of a $z_{phot} \approx 3.3$, massive galaxy selected from the NMBS, namely, C1-23152. We confirmed (1) the redshift of the source through the analysis of several nebular emission lines, and (2) the very large stellar mass of the galaxy by performing stellar population modeling of the SED of the galaxy corrected for both emission lines and AGN continuum. We also determined through analysis of emission-

[14] When including a central point-source component with fixed magnitude constrained by the maximal contribution from the AGN continuum to the observed SED as derived in Section 3.5, the sizes increase to $r_{e,circ} = 1.49$–1.73 kpc in the I_{814} and $r_{e,circ} = 1.05$–1.18 kpc in the H_{160} band, consistent within 2σ with the sizes obtained without a central point-like component.

line luminosities and line ratio diagnostics that C1-23152 likely hosts a luminous hidden AGN.

We found that C1-23152 is a very compact ($r_e \approx 1$ kpc), very massive ($\log(M_*/M_\odot) \gtrsim 11.3$) galaxy at $z_{spec} = 3.351$ with a formation redshift of $z \gtrsim 4$ with suppressed star formation, about to enter a post-starburst phase (as evidenced from the derived sSFR of $\log(\mathrm{sSFR/yr^{-1}}) \sim -11$). We used both BC03 and MA05 stellar population models along with the Calzetti et al. (2000) extinction law and a Kroupa (2001) IMF with varying SFH to model the observed SED. We found that independently of SED-modeling assumptions, the best-fit attenuation is consistent with zero, the timescale of the burst (τ) is very short (~50 Myr), and the SFR is low (3σ upper limit is $7\,M_\odot$ yr^{-1}). The low SFR inferred from SED fits is inconsistent with the SFRs derived from both $L_{[O\,II]}$ (and only marginally consistent when the [O II] luminosity is corrected for AGN contamination) and the observed MIPS 24 μm flux if the 24 μm detection is assumed to be due to dust-enshrouded star formation (by at least two orders of magnitude). The effect of different modeling assumptions changes the derived stellar mass by at most ± 0.08 dex. However, the estimated stellar age ($\langle t \rangle_{SFR} \sim 350$ Myr when adopting the BC03 models and a best-fit solar metallicity) is much more sensitive to the different SED-modeling assumptions, with the stellar age a factor of ~2 smaller when adopting the MA05 models. We find strong evidence for the presence of a luminous hidden AGN ($L_{bol,AGN} \sim 10^{46}$ erg s^{-1}), potentially responsible for the quenching of the star formation. We employed the observed relation between MIR and X-ray luminosities and bolometric corrections using high-z AGN templates to estimate the rest-frame $L_{2-10\,keV}$ but cannot conclude with certainty whether the non-detection of C1-23152 in the X-ray is due to flux limitations of the data or a Compton-thick nature of the AGN.

Independent constraints on the mass of C1-23152 can be obtained from its kinematics. Using the velocity dispersion derived from the [O III] line emission, we can attempt to estimate the dynamical mass of the galaxy using $M_{dyn} = C\sigma^2 r_e$, where C is a constant that depends on the structure of the galaxy and other parameters, and varies between $\log C = 5.87$ (the value resulting in $M_{dyn} \sim M_\odot$ for galaxies in the SDSS; Franx et al. 2008) and $\log C = 6.07$ (derived from kinematic data of local early-type galaxies; van Dokkum & Stanford 2003). Using the measurements of the effective radius from the H_{160} and the I_{814} bands, we estimated a dynamical mass ranging from $\log(M_{dyn}/M_\odot) = 10.91 \pm 0.24$ (adopting $\log C = 5.87$ and $r_e = 0.97$ kpc) to $\log(M_{dyn}/M_\odot) = 11.28 \pm 0.24$ (adopting $\log C = 6.07$ and $r_e = 1.45$ kpc), marginally consistent with stellar mass derived from the SED modeling. We note, however, that this calculation assumes that the [O III] line is a reasonable probe of the overall gravitational potential of the galaxy. Whereas this assumption is plausible if the [O III] emission originates from star formation and its line width is integrated over the entire galaxy, this does not appear to be the case for C1-23152, as the [O III] emission appears to be mostly produced by the AGN narrow line regions. Velocity dispersion measurements from stellar absorption lines are therefore needed to robustly derive the dynamical mass of C1-23152.

Our findings for the properties of this galaxy fit well into the scenario for the formation of the progenitors of local giant elliptical galaxies proposed by Marchesini et al. (2014). Marchesini et al. (2014) studied the evolution of the properties of the progenitors of local UMGs in the last 11.4 Gyr since $z = 3$, finding that at $2.5 < z < 3.0$ a small fraction (~15%) of the progenitors are already quiescent, implying that the assembly of the very massive end of the local quiescent red-sequence population must have started at $z > 3$. The stellar population properties (i.e., stellar age, star formation rate, rest frame colors) of C1-23152 are qualitatively and quantitatively consistent with it being the progenitor of the already quiescent progenitors of local UMGs at $z = 2.75$, as clearly evident in Figure 6, which shows the relative position in the UVJ diagram of C1-23152 and the quiescent progenitors at $2.5 < z < 3.0$ of local UMGs from Marchesini et al. (2014) (red points in Figure 6). Furthermore, Figure 6 clearly shows that the difference in age between C1-23152 and the quiescent progenitors at $2.5 < z < 3.0$ of local UMGs is quantitatively consistent with the cosmic time between $z = 3.35$ and $z \approx 2.5-3$.

The large stellar surface densities observed in C1-23152 and other massive galaxies at $z = 2-3$ imply that they must have formed via rapid, highly dissipative events at earlier times to account for the relatively small half-light radii and high Sérsic index n (Weinzirl et al. 2011). Although the exact physical picture underlying dissipative collapse mechanisms is uncertain (e.g., mergers, tidal interactions, Khochfar & Silk 2006; Hopkins et al. 2008; Bournaud et al. 2011; Perret et al. 2014; gas instabilities in turbulent diffuse disks, Kereš et al. 2005, 2009; Dekel et al. 2009; Ricciardelli et al. 2010; Dekel & Burkert 2014, cold gas accretion from intergalactic medium, Sales et al. 2012; Johansson et al. 2012), there is evidence that the radial gas inflows lead to centrally concentrated starbursts (Mihos & Hernquist 1994; Ellison et al. 2010; Scudder et al. 2012), along with fueling the central supermassive black holes (SMBH). The subsequent energetic feedback from the active SMBH may be sufficient to regulate and quench star formation by preventing gas cooling (Kauffmann & Haehnelt 2000; Croton et al. 2006; Hopkins et al. 2008; van de Voort et al. 2011). Given the correlations between black hole mass, bulge mass, and n (Peng et al. 2006; Graham & Driver 2007; Gültekin et al. 2009), our findings that C1-23152 is a very massive and compact galaxy with high n undergoing a post-starburst phase with evidence for a hidden luminous quasar support this scenario. The relatively short lifetime of the quenching phase (Mendel et al. 2013) also justifies the low likelihood of observing galaxies in the same transitional phase as C1-23152.

Simulations have shown that the formation of compact stellar systems must involve highly dissipational mechanisms on short timescales, consistent with stellar archeology studies of local massive ellipticals (Thomas et al. 2005). Gas-rich major mergers at high redshift serve as plausible examples for such a scenario (Wuyts et al. 2010). As gas is driven to the center, a massive nuclear starburst is ignited followed by an AGN/QSO phase that halts star formation, and leaving a compact stellar component. SMGs have been proposed as candidates to the above scenario (Toft et al. 2007; Cimatti et al. 2008; Schinnerer et al. 2008; Michalowski et al. 2010; Smolčić et al. 2011; Toft et al. 2014). While the mean size (Tacconi et al. 2006) and dynamical masses (Ivison et al. 2011) of SMGs measured through molecular lines have been found to be consistent with the properties of quiescent galaxies at $z \sim 2$ (e.g., Krogager et al. 2013; Toft et al. 2012),

there remains the challenge of robustly constraining the stellar masses of these systems (Michalowski et al. 2012).

Recently, Gilli et al. (2014) presented the study of an ultraluminous infrared galaxy at $z = 4.75$ in the Chandra Deep Field South, namely, XID 403. This source is found to be compact ($r \sim 0.9$ kpc), with a stellar mass estimated between $<3 \times 10^{10}\,M_{\odot}$ (de Breuck 2014) and $\sim 7 \times 10^{10}\,M_{\odot}$ (Gilli et al. 2014), depending on the amount of AGN contamination assumed in the rest-frame UV-to-NIR, and harboring a Compton-thick QSO. The SFR derived by fitting the far-IR SED is $\sim 650\,M_{\odot}\,\mathrm{yr}^{-1}$ (assuming Kroupa 2001 IMF), whereas fitting the optical/NIR SED results in SFR $\sim 180\,\mathrm{M}_{\odot}\ \mathrm{yr}^{-1}$ (Gilli et al. 2014). The inferred stellar mass, size, gas depletion timescale ($\sim 10^7$ yr), and SFR of XID 403 are consistent with it likely being the progenitor of the compact, quiescent, massive galaxies at $z < 3$. Our findings indicate that C1-23152 represents the transitioning phase between XID 403 and the compact, massive, quiescent galaxies at $z < 3$. Its quenched star formation activity while still harboring a hidden luminous AGN makes C1-23152 a natural descendent of XID 403. Furthermore, Straatman et al. (2014), studying massive, quiescent $z \sim 4$ galaxies, have shown that based on number density considerations, the majority of the star formation in their progenitors could have been obscured by dust. With an intense burst of star formation in the recent past of C1-23152, one may expect a significant amount of dust in C1-23152 as produced by supernovae. The upper limits on the amount of dust obscuration resulting from the SED modeling ($A_V < 0.4$ mag) seem to imply that the mechanism responsible for the quenching of star formation in C1-23152 may also be responsible for the destruction of most of the dust produced in the intense starburst that produced the very large stellar mass of C1-23152. However, in order to form conclusive and convincing evolutionary paths for the progenitors of post-starburst massive galaxies at $z \sim 3-4$, it is critical to investigate such scenarios by directly selecting progenitors by the use of some tracer, such as fixed number density or abundance matching (Behroozi et al. 2013; Marchesini et al. 2014), or fixed velocity dispersion (Bezanson et al. 2012; Belli et al. 2014a, 2014b). In particular, finding clear and direct evidence linking C1-23152 and compact, dusty star-forming galaxies at higher redshifts (such as the SMG studied in Gilli et al. 2014, see also Nelson et al. 2014, or $z > 3$ analogues of SF progenitors studied in Patel et al. 2013; Barro et al. 2014; Stefanon et al. 2014; Williams et al. 2014) would result in important constraints on timescales of dust formation and destruction.

A few insights can be derived regarding the evolution of C1-23152 and the progenitors of local UMGs at $2.5 < z < 3.0$ when examining Figure 6. The SF progenitors are predominantly found to be red in both $U - V$ and $V - J$ colors, indicating that they are dust obscured. Following the color evolution of local UMG progenitors in Marchesini et al. (2014) to $z \sim 1.25$, when all SF progenitors are quenched, the region typically populated by post-starburst galaxies in the $U - V$ versus $V - J$ diagram is not re-populated, indicating that SF progenitors at $z < 3$ appear to quench without losing dust, or quenching occurs significantly more rapidly than the destruction or removal of dust. The fact that there also exists a clear population of post-starburst galaxies at $z > 3$ with properties similar to C1-23152 (e.g., overall SED shape, SFR, and dust extinction) with short star formation timescales and little to moderate dust extinction implies that there are multiple paths for star-forming galaxies to join the quiescent population, characterized by different relative timescales responsible for quenching and dust removal.

Wellons et al. (2014), examining galaxies with properties similar to those of compact, massive quiescent galaxies observed at $z \sim 2$ with the Illustris cosmological simulation, find that there are multiple pathways to their formation. The dominant mechanisms responsible for the formation of this compact population are found to be either assembling at early times or through experiencing central starburst. Galaxies that assemble at early cosmic epochs when the gas density of the universe is very dense are formed compact and remain so, whereas galaxies that experience a central starburst (usually triggered through gas-rich mergers) become compact at later times ($z = 2$–4). While it is possible that both mechanisms play a role to a degree in the formation and evolution of galaxies similar to C1-23152, it is essential to disentangle the more dominant mechanism. Observationally, comparing the sizes of galaxies at different wavelengths can serve as a test (with those experiencing central starbursts having smaller sizes at shorter wavelengths and vice versa). Investigating the observational effects of dust for the different formation mechanisms in simulations is crucial, as it will provide insight into the color evolution of compact massive galaxies, perhaps explaining the multiple quenching modes of UMG progenitors discussed above.

Spectroscopic observations in both the optical and the NIR of other candidates of very massive galaxies at $z > 3$ are of vital importance to confirm their redshifts, to better characterize the properties of their stellar populations, to distinguish between dust-enshrouded star formation and highly obscured AGN activity, and to determine emission-line and AGN contamination to the SEDs and mass-to-light ratios. High-S/N rest-frame optical spectroscopy (especially redward of $\lambda_{\mathrm{rest}} \sim 5000$ Å) is needed to constrain SFH, SFRs, and metallicities, and to derive dynamical masses from stellar absorption lines for candidates of very massive galaxies in the first 2 Gyr of cosmic history (i.e., $z > 3$). NIRSpec on the *James Webb Space Telescope* will provide the instrumental capabilities and sensitivities to successfully target stellar-mass complete samples of these candidates and to comprehensively understand the population of monster galaxies in the early universe. Observations with the *Atacama Large Millimeter Array* will also be crucial in discriminating between dust-enshrouded star formation and obscured AGN activity, as well as providing an independent estimate of the dynamical masses of the most massive galaxies through measurements of the kinematics in these systems. Finally, current X-ray data are inconclusive as to whether the non-detection of C1-23152 in the X-ray is due to observational flux limitations or a Compton-thick nature of the AGN hosted in C1-23152. In order to constrain the column density of X-ray absorbing matter, and hence whether the AGN is Compton-thick, observations in both soft and hard bands are necessary. *The Nuclear Spectroscopic Telescope Array Mission* (NuSTAR; Harrison et al. 2013) will provide an opportunity to attempt addressing this issue.

We thank Marjin Franx and Ivan Valtchanov for valuable comments. Z.C.M. gratefully acknowledges support from the John F. Burlingame and the Kathryn McCarthy Graduate Fellowships in Physics at Tufts University. D.M. and Z.C.M. acknowledge the support of the Research Corporation for

Science Advancement's Cottrell Scholarship, the support from Tufts University Mellon Research Fellowship in Arts and Sciences, support from the programs *HST*-GO-12990 and *HST*-GO-12177.16, provided by NASA through a grant from the Space Telescope Science Institute, which is operated by the Association of Universities for Research in Astronomy, Incorporated, under the NASA contract NAS5-26555, and support by the National Aeronautics and Space Administration under Grant NNX13AH38G issued through the 12-ADAP12-0020 program. M.S. acknowledges support from the programs *HST*-GO-12286.11 and 12060.95. A.M. acknowledges support from the Netherlands Foundation for Research (NWO) Spinoza grant. A.F.S. acknowledges support from the Spanish Ministry for Economy and Competitiveness and FEDER funds through grants AYA2010-22111-C03-02 and AYA2013-48623-C2-2, and Generalitat Valenciana projects Prometeo 2009/064 and PROMETEO II/2014/060. A.K. acknowledges support by the Collaborative Research Council 956, sub-project A1, funded by the Deutsche Forschungsgemeinschaft (DFG). The Dark Cosmology Centre is funded by the Danish National Research Foundation. This study is partially based on data products from observations made with ESO Telescopes at the La Silla Paranal Observatory under programme ID 087.A-0514. Some of the data presented in this study were obtained at the W. M. Keck Observatory, which is operated as a scientific partnership among the California Institute of Technology, the University of California, and the National Aeronautics and Space Administration. The Observatory was made possible by the generous financial support of the W. M. Keck Foundation. Keck telescope time was granted by NOAO, through the Telescope System Instrumentation Program (TSIP). TSIP is funded by NSF. The authors wish to recognize and acknowledge the very significant cultural role and reverence that the summit of Mauna Kea has always had within the indigenous Hawaiian community. We are most fortunate to have the opportunity to conduct observations from this mountain. Also based on observations made with the Gran Telescopio Canarias (GTC), installed in the Spanish Observatorio del Roque de los Muchachos of the Instituto de Astrofísica de Canarias, in the island of La Palma. This study makes use of data from the NEWFIRM Medium-Band Survey, a multi-wavelength survey conducted with the NEWFIRM instrument at the KPNO, supported in part by the NSF and NASA. We thank the NMBS and COSMOS collaborations for making their catalogs publicly available. This work is also partially based on observations taken by the 3D-*HST* Treasury Program (GO 12177 and 12328) with the NASA/ESA *HST*, which is operated by the Association of Universities for Research in Astronomy, Inc., under NASA contract NAS5–26555. IRAM is supported by INSU/CNRS (France), MPG (Germany), and IGN (Spain). This work was supported through NSF ATI grants 1020981 and 1106284.

REFERENCES

Alexandroff, R., Strauss, M. A., Greene, J. E., et al. 2013, MNRAS, 435, 3306
Aretxaga, I., Wilson, G. W., Aguilar, E., et al. 2011, MNRAS, 415, 3831
Baldwin, J. A., Phillips, M. M., & Terlevich, R. 1981, PASP, 93, 5
Barro, G., Faber, S. M., Pérez-González, P. G., & Pablo, G. 2013, ApJ, 765, 104
Barro, G., Faber, S. M., Pérez-González, P. G., et al. 2014, ApJ, 791, 52
Behroozi, P. S., Marchesini, D., Wechsler, R. H., et al. 2013, ApJ, 777, 10
Bell, E. F., van der Wel, A., Papovich, C., et al. 2012, ApJ, 753, 167
Belli, S., Newman, A. B., & Ellis, R. S. 2014a, ApJ, 783, 117
Belli, S., Newman, A. B., Ellis, R. S., et al. 2014b, ApJL, 788, L29
Berti, S., Magnelli, B., Nordon, R., et al. 2011, A&A, 532, A49
Bezanson, R., van Dokkum, P. G., & Franx, M. 2012, ApJ, 760, 62
Bezanson, R., van Dokkum, P. G., Tal, T., et al. 2009, ApJ, 697, 1290
Bezanson, R., van Dokkum, P. G., & van de Sande, J. 2013, ApJ, 779, 21
Bournaud, F., Chapon, D., Teyssier, R., et al. 2011, ApJ, 730, 4
Brammer, G., van Dokkum, P. G., Franx, M., et al. 2012, ApJS, 200, 13
Brammer, G. B., van Dokkum, P. G., & Coppi, P. 2008, ApJ, 686, 1503
Brammer, G. B., Whitaker, K. E., van Dokkum, P. G., et al. 2011, ApJ, 739, 24
Bruzual, G., & Charlot, S. 2003, MNRAS, 344, 1000
Calzetti, D., Armus, L., Bohlin, R. C., et al. 2000, ApJ, 533, 682
Capak, P., Aussel, H., Ajiki, M., et al. 2007, ApJS, 172, 99
Casey, C. M. 2012, MNRAS, 425, 3094
Casey, C. M., Chen, C., Cowie, L. L., et al. 2013, MNRAS, 436, 1919
Cepa, J., Aguiar, M., Bland-Hawthorn, J., et al. 2003, in RMxAA Conf. Ser. 16, ed. J. M. Rodriguez Espinosa, F. Garzon Lopez, & V. Melo. Martin, 13
Chang, Y. Y., van der Wel, A., Rix, H.-W., et al. 2013, ApJ, 773, 149
Charlot, S., Brinchmann, J., & White, S. D. M. 2006, MNRAS, 370, 1106
Cimatti, A., Cassata, P., Pozzetti, L., et al. 2008, A&A, 482, 21
Conroy, C., Dutton, A. A., Graves, G. J., et al. 2013, ApJ, 776, 26
Conroy, C., & Gunn, J. E. 2010, ApJ, 712, 833
Conroy, C., Gunn, J. E., & White, M. 2009, ApJ, 699, 486
Conroy, C., & van Dokkum, P. 2012, ApJ, 760, 71
Conroy, C., White, M., & Gunn, J. E. 2010, ApJ, 708, 58
Cowie, L. L., Songaila, A., & Hu, E. H. 1996, AJ, 112, 839
Croton, D. J., Springer, V., White, S. D., et al. 2006, MNRAS, 365, 11
Daddi, E., Cimatti, A., Renzini, A., et al. 2004, ApJL, 600, 127L
Daddi, E., Renzini, A., Pirzkal, N., et al. 2005, ApJ, 626, 680
Dale, D. A., & Helou, G. 2002, ApJ, 576, 159
Dale, D. A., Helou, G., Magdis, G. E., et al. 2014, ApJ, 784, 83
De Breuck, C., et al. 2014, A&A, 565, A59
Dekel, A., & Burkert, A. 2014, MNRAS, 438, 1870
Dekel, A., Sari, R., Ceverinp, D., et al. 2009, ApJ, 703, 785
D'Odorico, S., Dekker, H., Mazzoleni, R., et al. 2006, Proc. SPIE, 6269, 98
Dopita, M. A., Firschera, J., & Sutherland, R. S. 2006, ApJ, 647, 244
Ellison, S. L., Patton, D. R., Simard, L., et al. 2010, MNRAS, 407, 1514
Elvis, M., et al. 2009, ApJS, 184, 158
Finkelstein, K. D., Papovich, C., Finkelstein, S. L., et al. 2011, ApJ, 742, 108
Floyd, D. J. E., Dunlop, J. S. D., Kukula, M. J., et al. 2013, MNRAS, 429, 2
Fontanot, F., de Lucia., G., Monaco, P., et al. 2009, MNRAS, 397, 1776
Föster Scheriber, N. M., van Dokkum, P. G., Franx, M., et al. 2004, ApJ, 616, 40
Franx, M., van Dokkum, P. G., Schreiber, N. M., et al. 2008, ApJ, 688, 770
Fu, H., Cooray, A., Feruglio, C., et al. 2013, Natur, 498, 338
Gandhi, P., Horst, H., Smette, A., et al. 2009, A&A, 502, 457
Geier, S., Richard, J., Man, A. W. S., et al. 2013, ApJ, 777, 87
Gilli, R., Norman, C., Vignali, C., et al. 2014, A&A, 562, 67
Goldoni, P. 2011, AN, 332, 227
Graham, A. W., & Driver, S. P. 2007, ApJ, 655, 77
Gültekin, K., Richstone, D. O., Mo, H. J., et al. 2009, MNRAS, 398, 1129
Hainline, K. N., Shapley, A. E., Greene, J. E., et al. 2011, ApJ, 733, 31
Hall, P. B., Hoversten, E. A., Tremonti, C. A., et al. 2004, AJ, 128, 3148
Hao, L., Strauss, M. A., Fan, X., et al. 2005, AJ, 129, 1783
Harrison, F. A., Craig, W. W., Christensen, F. E., et al. 2013, ApJ, 770, 103
Holden, B. P., Oesch, P. A., Gonzalez, V. G., et al. 2014, ApJ, submitted
Holland, W. S., Bintley, D., Chapin, E. L., et al. 2013, MNRAS, 430, 2513
Hopkins, P. F., Hernquist, L., Cox, T. J., & Keres, D. 2008, ApJS, 175, 356
Hopkins, P. F., Richards, G. T., & Hernquist, L. 2007, ApJ, 654, 731
Horne, K. 1986, PASP, 98, 609
Ilbert, O., McCracken, H. J., le Févre, O., et al. 2013, A&A, 556, 55
Ivison, R. J., Papadopoulos, P. P., Smail, I., et al. 2011, MNRAS, 412, 1913
Ivison, R. J., Swinbank, A. M., Smail, I., et al. 2013, ApJ, 772, 137
Johansson, P. H., Naab, T., & Ostriker, J. P. 2012, ApJ, 754, 115
Juneau, S., Bournaud, F., Charlot, S., et al. 2014, ApJ, 788, 88
Juneau, S., Dickinson, M., Alexander, D. M., & Salim, S. 2011, ApJ, 736, 104
Kauffmann, G., Colberg, J. M., Diaferio, A., et al. 1999, MNRAS, 307, 529
Kauffmann, G., & Haehnelt, M. 2000, MNRAS, 311, 576
Kauffmann, G., & White, S. D. M. 1993, MNRAS, 261, 921
Kennicutt, R. C., Jr. 1998, ARA&A, 36, 189
Kereš, D., Kats, N., Fardal, M., et al. 2009, MNRAS, 395, 160
Kereš, D., Kats, N., Weinberg, D. H., et al. 2005, MNRAS, 363, 2
Kewley, L. J., Geller, M. J., & Jansen, R. A. 2004, AJ, 127, 2002
Kewley, L. J., Groves, B., Kauffmann, G., & Heckman, T. 2006, ApJ, 372, 961
Khochfar, S., & Silk, J. 2006, MNRAS, 370, 902

Kirkpatrick, A., Pope, A., Alexander, D. M., et al. 2012, ApJ, 759, 139
Koekemoer, A. M., Fruchter, A. S., Hook, R. N., & Hack, W. 2002, in The 2002 *HST* Calibration Workshop, ed. S. Arribas
Kriek, M., van Dokkum, P. G., Labbé, I., et al. 2009, ApJ, 700, 221
Krogager, J.-K., Zirm, A. W., Toft, S., et al. 2013, arXiv:1309.6316
Kroupa, P. 2001, MNRAS, 322, 231
Kuiper, E., Hatch, N. A., Miley, G. K., et al. 2011, MNRAS, 415, 2245
Kulas, K. R., Shapley, A. E., Kollmeier, J. A., et al. 2012, ApJ, 754, 33
Kummel, M., Rosati, P., Fosbury, R., et al. 2011, A&A, 530, 86
Kummel, M., Walsh, J. R., Pirzkal, N., et al. 2009, PASP, 121, 59
Labbé, I., Huang, J., Franx, M., et al. 2005, ApJ, 624, L81
Lamastra, A., Bianchi, S., Matt, G., et al. 2009, A&A, 504, 73
Lemaux, B. C., Lubin, L. M., Shapley, A., et al. 2010, ApJ, 716, 970
Lutz, D., Poglitsch, A., Altieri, B., et al. 2011, A&A, 532, 90
Magdis, G. E., Daddi, E., Béthermin, M., et al. 2012, ApJ, 760, 6
Mancini, C., Matute, I., Cimatti, A., et al. 2009, A&A, 500, 705
Maraston, C. 2005, MNRAS, 362, 799
Marchesini, D., Muzzin, A., Stefanon, M., et al. 2014, ApJ, 794, 65
Marchesini, D., van Dokkum, P. G., Föster Schreiber, N. M., et al. 2009, ApJ, 701, 1765
Marchesini, D., Whitaker, K. E., Brammer, G., et al. 2010, ApJ, 725, 1277
Marconi, A., Risaliti, G., Gilli, R., et al. 2004, MNRAS, 351, 169
Martin, D. C., Fanson, J., Schiminovich, D., et al. 2005, ApJL, 619, L1
Maschietto, F., Hatch, N. A., Venemans, B. P., et al. 2008, MNRAS, 389, 1223
McCracken, H. J., Capak, P., Salvato, M., et al. 2010, ApJ, 708, 202
McLean, I. S., Becklin, E. E., Bendiksen, O., et al. 1998, SPIE, 3354, 566
McLinden, E., Finkelstein, S. L., Rhoads, J. E., et al. 2011, ApJ, 730, 136
Mendel, J. T., Simard, L., Ellison, S. L., & Patton, D. R. 2013, MNRAS, 429, 2212
Michalowski, M., Hjorth, J., & Watson, D. 2010, A&A, 514, 67
Michalowski, M. J., Dunlop, J. S., Cirasuolo, M., et al. 2012, A&A, 541, 85
Mihos, J. C., & Hernquist, L. 1994, ApJ, 425, L13
Modigliani, A., Goldoni, P., Royer, F., et al. 2010, Proc. SPIE, 7737, 56
Muzzin, A., Marchesini, D., Stefanon, M., et al. 2013a, ApJS, 206, 8
Muzzin, A., Marchesini, D., Stefanon, M., et al. 2013b, ApJ, 777, 18
Naab, T., Khochfar, S., & Burkert, A. 2006, ApJL, 636, L81
Nakajima, K., Ouchi, M., Shimasaku, K., et al. 2013, ApJ, 769, 3
Nandra, K., & Pounds, K. A. 1994, MNRAS, 268, 405
Nelson, E., van Dokkum, P., Franx, M., et al. 2014, Natur, 513, 394
Norman, C., Hasinger, G., Giacconi, R., et al. 2002, ApJ, 571, 218
Oliver, S. J., Bock, J., Altieri, B., et al. 2012, MNRAS, 424, 1614
Papovich, C., Finkelstein, S. L., Ferguson, H. C., et al. 2011, MNRAS, 412, 1123
Patel, S. G., Holden, B. P., Kelson, D. D., et al. 2012, ApJL, 748, L27
Patel, S. G., van Dokkum, P. G., Franx, M., et al. 2013, ApJ, 766, 15
Peng, C. Y., Ho, L. C., Impey, C. D., et al. 2002, ApJ, 124, 266
Peng, C. Y., Impey, C. D., Rix, H.-W., et al. 2006, ApJ, 649, 616
Pérez-González, P. G., Rieke, G. H., Villar, V., et al. 2008, ApJ, 675, 234
Perret, V., Renaud, F., Epinat, B., et al. 2014, A&A, 562, A1
Pettini, M., Shapley, A. E., Steidel, C. C., et al. 2001, ApJ, 554, 981
Polletta, M., Tajer, M., Maraschi, L., et al. 2007, ApJ, 663, 81
Rawlings, S., & Saunders, R. 1991, Natur, 349, 138
Ricciardelli, E., Trujillo, I., Buitrago, F., & Conselice, C. J. 2010, MNRAS, 406, 230
Richards, G. T., Kruczek, N. E., Gallagher, S. C., et al. 2011, ApJ, 141, 167
Rujopakarn, W., Rieke, G. H., Weiner, B. J., et al. 2013, ApJ, 767, 73
Sales, L. V., Navarro, J. F., Theuns, T., et al. 2012, MNRAS, 423, 1544
Salpeter, E. 1955, ApJ, 121, 161
Salvato, M., Hasinger, G., Ilbert, O., et al. 2009, ApJ, 690, 1250
Sanders, D. B., Salvato, M., Aussel, H., et al. 2007, ApJS, 172, 86
Schinnerer, E., Carilli, C. L., Capak, P., et al. 2008, ApJ, 689, 5
Schinnerer, E., Sargent, M. T., Bondi, M., et al. 2010, ApJS, 118, 384
Schinnerer, E., Smolčić, V., Carilli, C. L., et al. 2007, ApJS, 172, 46
Scott, K. S., Austermann, J. E., Perera, T. A., et al. 2008, MNRAS, 385, 2225
Scoville, N., Aussel, H., Brusa, M., et al. 2007, ApJS, 172, 1
Scudder, J. M., Ellison, S. L., Torrey, P., et al. 2012, MNRAS, 426, 549
Shen, S., Mo, H. J., White, S. D. M., et al. 2003, MNRAS, 343, 978
Silverman, J. D., Lamareille, F., Maier, C., et al. 2009, ApJ, 696, 396
Skelton, R. E., Whitaker, K. E., Momcheva, I. G., et al. 2014, ApJS, 214, 24
Smail, I., Ivison, R. J., Blain, A. W., et al. 2002, MNRAS, 331, 495
Smolčić, V., Capak, P., Ilbert, O., et al. 2011, ApJ, 731, 27
Spiniello, C., Trager, S., Koopmans, L. V. E., et al. 2014, MNRAS, 438, 1483
Spitler, L. R., Straatman, C. M. S., Labbé, I., et al. 2014, ApJ, 787, 36
Spoon, H. W. W., Farrah, D., Lebouteiller, V., et al. 2013, ApJ, 775, 127
Straatman, C. M. S., Labbé, I., Spitler, L. R., et al. 2014, ApJL, 783, L14
Strazzullo, V., Gobat, R., Daddi, E., et al. 2013, ApJ, 772, 118
Stefanon, M., Marchesini, D., Muzzin, A., et al. 2014, ApJ, submitted
Stefanon, M., Marchesini, D., Rudnick, D., et al. 2013, ApJ, 768, 92
Tacconi, L. J., Neri, R., Chapman, S. C., et al. 2006, ApJ, 640, 228
Taniguchi, Y., Scoville, N., Murayama, T., et al. 2007, ApJS, 172, 9
Teplitz, H. I., McLean, I. S., Becklin, E. E., et al. 2000, ApJ, 533, L65
Thomas, D., Maraston, C., Bender, R., & Mendes de Oliveira, C. 2005, ApJ, 621, 673
Thomas, D., Maraston, C., Schawinski, K., Sarzi, M., & Silk, J. 2010, MNRAS, 404, 1775
Toft, S., Gallazzi, A., Zirm, A., et al. 2012, ApJ, 754, 3
Toft, S., Smolo˘cić, V., Magnelli, B., et al. 2014, ApJ, 782, 68
Toft, S., van Dokkum, P., Franx, M., et al. 2007, ApJ, 671, 285
Tremonti, C. A., Heckman, T. M., Kauffmann, G., et al. 2004, ApJ, 613, 898
Trujillo, I., Feulner, G., Goranova, Y., et al. 2006, MNRAS, 373, 36
Trujillo, I., Conselice, C. J., Bundy, K., et al. 2007, MNRAS, 381, 109
Trujillo, I., Ferreras, I., & de La Rosa, I. G. 2011, MNRAS, 415, 3903
Valdes, F. 1992, ASPC, 417, 25
van De Sande, J., Kriek, M., Franx, M., et al. 2013, ApJ, 771, 85
van de Voort, F., Schaye, J., Booth, C. M., et al. 2011, MNRAS, 415, 2782
van der Wel, A., Franx, M., van Dokkum, P. G., et al. 2014, ApJ, 788, 28
van der Wel, A., Holden, B. P., Zirm, A. W., et al. 2008, ApJ, 688, 48
van Dokkum, P. G. 2001, PASP, 113, 1420
van Dokkum, P. G., Brammer, G., Fumagalli, M., et al. 2011, ApJ, 743L, 15
van Dokkum, P. G., Franx, M., Kriek, M., et al. 2008, ApJ, 677, 5
van Dokkum, P. G., Labbé, I., Marchesini, D., et al. 2009, PASP, 121, 2
van Dokkum, P. G., & Stanford, S. A. 2003, ApJ, 585, 78
van Dokkum, P. G., Whitaker, K., Brammer, G., et al. 2010, ApJ, 709, 1018
Verhamme, A., Schaerer, D., & Maselli, A. 2006, A&A, 460, 397
Wake, D. A., van Dokkum, P. G., & Franx, M. 2012, ApJL, 751, L44
Walter, F., Decarli, R., Carilli, C., et al. 2012, Natur, 486, 233
Weinzirl, T., Jogee, S., Conselice, C. J., et al. 2011, ApJ, 743, 87
Wellons, S., Torrey, P., Ma, C., et al. 2014, MNRAS, submitted
Whitaker, K. E., Labbé, I., van Dokkum, P. G., et al. 2011, ApJ, 735, 86
White, S. D., & Frenk, C. S. 1991, ApJ, 379, 52
White, S. D., & Rees, M. J. 1978, MNRAS, 183, 341
Wiklind, T., Dickinson, M., Ferguson, H. C., et al. 2008, ApJ, 676, 781
Williams, C. C., Giavalisco, M., Cassata, P., et al. 2014, ApJ, 780, 1
Williams, R. J., Quadri, R. F., Franx, M., et al. 2009, ApJ, 691, 1879
Wuyts, S., Cox, T. J., Hayward, C. C., et al. 2010, ApJ, 722, 1666
Wuyts, S., Labbé, I., Franx, M., et al. 2007, ApJ, 655, 51
Wuyts, S., Förster Schreiber, N. M., Lutz, D., et al. 2011, ApJ, 738, 106
Zirm, A. W., van der Wel, A., Franx, M., et al. 2007, ApJ, 656, 66